

High Energy Lithium-ion Battery Characterisation and Overcharge Abuse Test

Master's thesis in Sustainable Energy Systems

AKHILESH SATISH PATIL

DEPARTMENT OF PHYSICS

CHALMERS UNIVERSITY OF TECHNOLOGY
Gothenburg, Sweden 2022

MASTER'S THESIS 2022

High Energy Lithium-ion Battery Characterisation and Overcharge Abuse Test

AKHILESH SATISH PATIL



CHALMERS
UNIVERSITY OF TECHNOLOGY

Department of Physics
CHALMERS UNIVERSITY OF TECHNOLOGY
Gothenburg, Sweden 2022

High Energy Lithium-ion Battery
Characterisation and Overcharge Abuse Test
AKHILESH SATISH PATIL

© AKHILESH SATISH PATIL, 2022.

Supervisors: Maurizio Furlani, Department of Physics
Fredrik Larsson, Alelion Energy Systems

Examiner: Bengt-Erik Mellander, Department of Physics

Master's Thesis 2022
Department of Physics
Chalmers University of Technology
SE-412 96 Gothenburg
Telephone +46 31 772 1000

Cover: The picture represents the event of gas emissions detected by the gas sensors across the thermal runaway one of the overcharge experiment. The plot is normalized to the range of the sensors vs time for different gas emissions.

Typeset in L^AT_EX
Printed by Chalmers Reproservice
Gothenburg, Sweden 2022

High Energy Lithium-ion Battery
Characterisation and Overcharge Abuse Test
AKHILESH SATISH PATIL
Department of Physics
Chalmers University of Technology

Abstract

Batteries are finding extensive applications in different domains. Lithium-ion batteries are one of the most interesting kinds. They are used in most of the portable electronic equipment, small and large appliances, electrical energy storage system and electric vehicles due to their high power and high energy densities. Nevertheless lithium-ion technology has its own dangers due to presence of highly volatile and flammable materials. These properties can lead to emissions of gas from the cell package, further leading to thermal runaway and toxic gas emissions. Many researches have reported that gas emissions include highly detrimental gases like hydrogen fluoride (HF), carbon monoxide (CO) as well as phosphoryl fluoride (POF₃).

The lithium-ion cell construction involves graphite based anode metal oxide cathode and a liquid electrolyte with high lithium ion mobility. Due to high electrochemical reactivity and mechanical degradation under different operative conditions, the battery will eventually lead to decreased performance. Cathodic materials limit the energy density and are the primary reason for the battery cost. Those materials being Nickel (Ni), Manganese (Mn) and Cobalt (Co) with lithium intercalating oxides. The different proportion of these metals can influence the performance levels in the batteries.

In this thesis, a number of methods have been used to characterize prismatic lithium-ion battery cells. The investigation has included analysis of the disassembled cell components using: thermal analysis for the separator material, X-ray diffraction (XRD) for electrode materials and Fourier transform infrared spectroscopy (FTIR) for liquid electrolyte analysis, gas analysis, as well as electrical measurements such as impedance, charge and discharge tests on the complete cell. Overcharge abuse tests have been performed to further investigate cell safety by analysing gas emissions using gas sensors, FTIR and physical parameters such as temperature across the thermal runaway in a cell fault scenario.

Keywords: Lithium-ion batteries, NMC, Overcharge, Abuse, Safety, Thermal runaway, gas emissions, FTIR, DSC, XRD

Acknowledgements

I would like to express my great many thanks to my examiner Professor Bengt-Erik Melander for giving the opportunity to carry out this thesis and providing the necessary support and leadership continuously to bring out the quality work and results from the project.

The assistance provided by my supervisor Dr.Maurizio Furlani is greatly appreciated. I got the opportunity to learn about several new things that influenced the content of the thesis in a constructive way.

I wish to extend my special thanks to Fredrik Larsson from Alelion Energy Systems for providing technical help which moved the project in a productive direction. Also, I wish to extend my thanks to FAB Detect AB for providing sensors for the gas measurements.

Akhilesh Patil, Gothenburg, Sep 2022

Contents

| | |
|--|-------------|
| Figures | vii |
| Tabels | viii |
| 1 Introduction | 1 |
| 1.1 The Lithium-ion cell | 2 |
| 1.2 The Battery system | 2 |
| 1.3 Lithium-ion cell chemistry | 3 |
| 1.3.1 Basic Construction | 3 |
| 1.3.2 Electrolytes | 3 |
| 2 Thesis Scope | 5 |
| 3 Experimental Overview | 6 |
| 3.1 IR Spectroscopy | 6 |
| 3.1.1 Absorbance | 7 |
| 3.1.2 Attenuated total reflection [ATR] | 8 |
| 3.2 Impedance Spectroscopy and Cycling | 9 |
| 3.3 Thermal Analysis | 11 |
| 3.4 X-Ray Diffraction | 12 |
| 4 Results and Discussion | 13 |
| 4.1 Electrical Characterisation | 13 |
| 4.2 Characterisation of battery materials | 14 |
| 4.2.1 Dismantling of the test cells | 14 |
| 4.2.2 Thermal Analysis [DSC] | 20 |
| 4.2.3 X-ray Diffraction [XRD] | 25 |
| 4.2.4 Fourier Transform Infrared Spectroscopy [FTIR] | 29 |
| 4.3 Abuse testing | 32 |
| 4.3.1 Outline of the experiment 1 results | 34 |
| 4.3.2 FTIR Spectrum analysis from experiment 1 | 37 |
| 4.3.3 Outline of the experiment 2 results | 38 |
| 4.3.4 FTIR Spectrum analysis from experiment 2 | 41 |
| 5 Conclusions | 44 |
| References | 46 |

Figures

| | | |
|----|---|----|
| 1 | Schematic of lithium-ion discharge. | 3 |
| 2 | Molecular structure of common electrolytes | 4 |
| 3 | Schematic of FTIR principle | 6 |
| 4 | Modifications made to the FTIR gas cell | 7 |
| 5 | Principle of attenuated total reflection | 8 |
| 6 | Schematic of FRA measurement. | 9 |
| 7 | Nyquist plot obtained from test cell 1 | 10 |
| 8 | Schematic of setup for cell cycling. | 10 |
| 9 | Section of DSC measuring cell. | 11 |
| 10 | Schematic of X-ray diffractor. | 12 |
| 11 | Comparison of charging and discharging cycle for test cell 1. | 13 |
| 12 | Schematic for cell discharge. | 14 |
| 13 | Test Cell 1 | 15 |
| 14 | Test Cell 2 | 16 |
| 15 | Test Cell 3 | 17 |
| 16 | Heat flow curves of separators. | 20 |
| 17 | Electrode Material X-ray Diffraction Patterns | 25 |
| 18 | ATR spectrum of liquid electrolyte extracted from test cell 1 | 29 |
| 19 | Transmission spectrum of liquid phase electrolyte | 31 |
| 20 | Schematic of the abuse test cite | 33 |
| 21 | Trace graphs of emissions during the experiment 1 | 34 |
| 22 | Gas emission FTIR spectrum from abuse test | 37 |
| 23 | Trace graphs of emissions during the experiment 2 | 38 |
| 24 | Gas emission FTIR spectrum from abuse test | 41 |

Tabels

| | | |
|---|---|----|
| 1 | Description of test cells | 5 |
| 2 | Parts of the DSC cell | 11 |
| 3 | Approximate dimensions of cell packaging | 19 |
| 4 | Onset temperatures of separator samples | 24 |
| 5 | Assignments of spectrum bands from ATR spectrum of extracted electrolyte out of test cell 1 at different evaporation time. | 30 |
| 6 | Ratings of the gas sensors | 32 |
| 7 | Assignments of spectrum bands from ATR spectrum of vented gas emissions from test cell 1 during abuse test | 43 |

1 Introduction

In order to tackle the climate change caused by increased anthropogenic activities, the carbon-intensive sectors should be given the utmost attention to reduce the carbon emissions. The current energy demand in the world is majorly fulfilled by fossil based systems. In order to reduce the carbon emissions and to achieve a fossil free society the advancements in lithium-ion batteries will play a key role. The employment of lithium-ion batteries in different sectors has already seen a rapid increase. The transportation sector is one of the major contributor of CO₂ emissions worldwide and electric vehicles (EVs) have a large potential to reduce these emissions. In order to achieve this at a faster rate, the major step would be to electrify the majority of the transport sector with the lithium-ion battery technology [1]. The electrification of transport sector and battery storage for complementing solar PV systems could have a significant role for sustainable energy systems. However the requirements are different for these applications, and the efficient design with high energy density and performance characteristics influenced by cycling and other operational issues are topics of interest in both. Repeated charge and discharge result, in the long term, degradation of the battery capacity. In addition, the rise in impedance as a result of early capacity fade will lead to decreased efficiency in terms of power supply and cause battery systems to eventually malfunction.

The challenges for incorporating large battery systems in a vehicle are continuously increasing. The employment of batteries in small passenger vehicles for electrical drivetrain is increasing constantly as a result of gradual phasing out of internal combustion vehicles, but for heavy duty and commercial vehicles it is still a large problem in shifting towards battery technology. The weight of the battery system and the range of the vehicle are a few issues to mention. These battery systems have limitations in terms of safety, longevity and performance. Although the safety standards are high there is an increased risk of fire and many incidents among electric vehicles (EVs) have been reported. For example, in June 2022, a Tesla model S caught fire three weeks after a crash in Sacramento [2]. Also plug-in hybrid electric vehicles (PHEVs) such as Fiskar Karma with relatively smaller battery also caught fire in a supermarket [3]. Since the application of battery systems is increasing for commercial vehicles including electric buses and trucks, the instances of fire accidents have come into light also for this category of vehicles. For example, in April 2022, an electric bus used for public transport caught fire in the city of Paris. These buses were manufactured by Bolloré, and incorporated six battery packs of solid state lithium-metal polymer type [4]. In an accidental case, a thermal runaway can lead to evaporation, venting and/or combustion of electrolyte, electrolyte-electrode reactions and so on [5]. Eventually developing a fire that can spread cell to cell propagating in the battery system. As a result, it can bring internal short circuit, . Further, the intense fire and heat from the battery system can cause highly toxic hydrogen fluoride (HF) and phosphoryl fluoride (POF₃) emissions. Toxic emissions and intensity of emissions in different types of abused lithium-ion cells have been partially described in the literature [6]. Hence it is an overriding aspect to study and analyse these issues to possibly increase the safety throughout the lifetime of batteries and have enough knowledge to be able to recover or reuse key materials from the spent batteries.

1.1 The Lithium-ion cell

The commercially available lithium-ion cells are mainly categorised in three types: Cylindrical hard metal, prismatic metal and pouch cell packaging. In cylindrical type the electrodes and separator are rolled together. These type of packaging have the disadvantage of non-uniform temperature distribution further leading to uneven aging between the layers. The prismatic metal cells have electrode strips wound and separators are sandwiched in between. On the other hand, in case of pouch type, single electrode sheets are stacked onto each other. The housings of hard metal cases are made of steel or deep-drawn aluminium plate in the cuboid form. The housing for pouch cells is deep drawn aluminium foil and a polymer compound. The packaging is comparatively complex for prismatic pouch type rather than prismatic hard case [7]. The prismatic cells are used in electric cars, off-road heavy duty vehicles and forklifts for their robustness and optimal packaging has allowed higher energy density and nominal capacity [8].

1.2 The Battery system

Several battery cells are electrically interconnected and placed in a rigid enclosure to reach voltage or capacity as required for the application. The interconnected cells form a battery system which requires a battery management system to monitor and maintain the electrical properties to keep the balance for all the cells in the system to minimize the risk of failure. The cells can be connected either in parallel or in series or both depending on the type of application by integrating into various cell modules. Further, these modules are incorporated into the battery pack. To increase the current, the battery packs can be connected in parallel and connected in series to increase the voltage. The charging process takes place with an external electric supply. For large systems, there is also a incorporated cooling system to ensure safe and optimal operation at different temperature conditions [9].

1.3 Lithium-ion cell chemistry

1.3.1 Basic Construction

The breakthrough for lithium-ion batteries was obtained in 1978 with the development of the so-called insertion or intercalation electrodes [10]. The compounds used to develop these electrodes, can reversibly accept and release lithium ions in and out of their open structure. to allow the continuation of the electro-chemical reaction as well as of the cycle life , the material must ensure a reversible evolution of both the electronic structure (to balance the positive charge of the inserted lithium ions) and of the crystal structure (to prevent the lattice collapsing) [11]. The basic construction of lithium-ion batteries involve two electrodes cathode (positive) and anode (negative) separated by an electrolyte containing lithium ions.

The electrons move from cathode to anode externally whereas the lithium ions move internally from cathode to anode with the help of the electrolyte. The reverse phenomena is seen during discharging process, that is lithium ions move from anode to the cathode through electrolyte. The shuttling of lithium ions from cathode and anode during charging and discharging is known as "shuttle chair" mechanism [12]. A separator made from polymer isolates the two electrodes to prevent the short circuit but allowing the exchange of lithium ions.

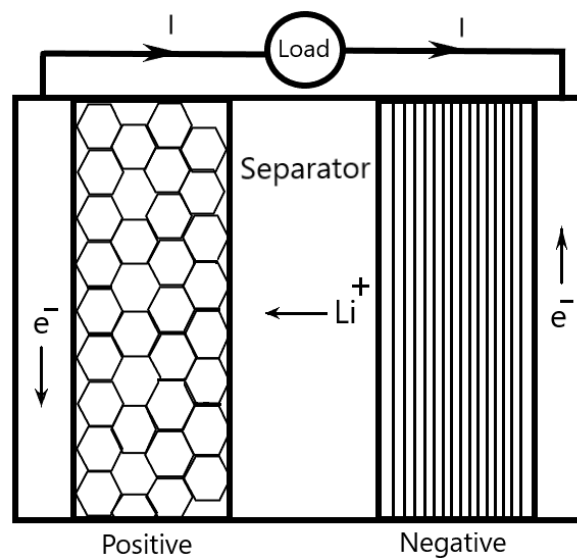
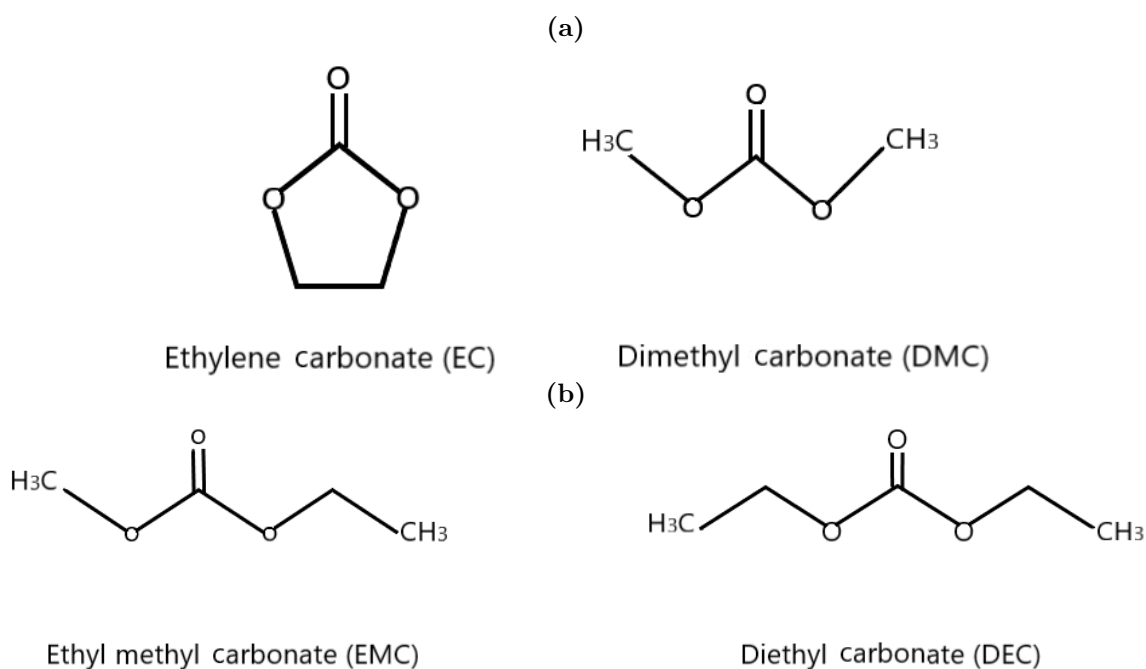


Figure 1: Schematic of lithium-ion discharge.

1.3.2 Electrolytes

The range of applications of electrolytes can be influenced by their electrochemical stability and ionic conduction and dielectric property. The dielectric constant is a property which gives information about the polarity of the molecules present in the electrolytes [13].

Figure 2: Molecular structure of common electrolytes

The present day electrolytes contain low molecular weight linear structured and cyclic organic solvents, typically carbonates (figures 2a and 2b). Ethylene carbonate (EC), propylene carbonate (PC) are mixed with ethyl methyl carbonate (EMC), dimethyl carbonate (DMC) or diethyl carbonate (DEC) [14] and vinyl carbonate (VC). Other possible solvents that can be used are ethyl acetate (EA) dimethoxy ethane (DME) [15]. EC and PC are substantially used for their low melting point, high boiling point and very high dielectric constant. While, linear carbonates even with a lower dielectric constant, contribute to the fluidity of EC leading to a better ionic conductivity. The salts containing lithium ions dissociate in the solvents and act as charge carriers during the charging and discharging process. LiPF_6 is the most used salt in present day applications.

2 Thesis Scope

The major part of the thesis work was carried out within Chalmers University of Technology and in co-operation with Alelion Energy Systems AB, a company specialised in customized modular battery systems. The firm supported the work with procurement of high energy lithium-ion battery cells for experimental investigations and facilities for abuse testing. The cells obtained were of prismatic hard case type designated as standard DIN 91252:2016-11 of three different capacities. The different test cells are as mentioned in table 1.

| Parameters | Test cell 1 | Test cell 2 | Test cell 3 |
|-------------------|-------------|-------------|-------------|
| Capacity (Ah) | 49.5 | 37 | 28 |
| Voltage limits(V) | 2.8-4.25 | 2.8-4.2 | 2.8-4.2 |

Table 1: Description of test cells

The aim of the thesis work is to analyze safety issues for the large capacity lithium-ion battery cells by electrical, thermal and gas emission studies under abuse situations and the possibility of recover or reuse of cell materials. The work includes postmortem analysis as well as the setup of suitable measurement systems. The thesis was divided into two major parts. First, to discharge the cells completely and dismantle them systematically to examine the construction and interior components of the packaging. Further, using Fourier Transform Infrared equipment to analyse liquid from the interior environment of the cell packaging. In addition, the X-Ray diffraction method was also used to conduct post-mortem studies of the anode and cathode of the test cells. Second, the testing of cells for electrical measurements by performing cell cycling and impedance spectroscopy using specialized laboratory equipment. Third, overcharge abuse tests were done and gas emissions were investigated by incorporating gas sensors and Fourier Transform Infrared Spectroscopy (FTIR).

3 Experimental Overview

3.1 IR Spectroscopy

The IR spectroscopy is used in this thesis to study the chemical structure of the electrolytes present in the lithium ion cells and the gas emissions. The sensitivity of the chemical compounds is based on their vibro-rotational energy, due to the changing dipole moment of the molecule due to vibrations or rotations, in the interaction with the infrared beam of energy. This principle is the basis for IR spectroscopy and results in the plot the different spectrum based on the different vibrational energy of the molecules [16]. The Fourier Transform IR (FTIR) spectroscopy is based on the interference pattern created by the alternating movement of the mirror that modify the path length of half of the beam. Our instrument has special setup compared to an ordinary Michelson Interferometer where the fixed mirror and movable mirror are connected in tandem to obtain the same resultant effect with much stability and portability. And, the instrument is coupled to a computer to conduct the fourier transform of the interferograms obtained. The computer and software carry out the numerical calculations and represents in a simpler interface of spectra for the users. The resolution and the spectral region can be defined while performing the experiment where a finer resolution implies longer analysis time. Current FTIR spectroscopy equipment can accommodate varied modifications and attachments to suit the distinct experiments.

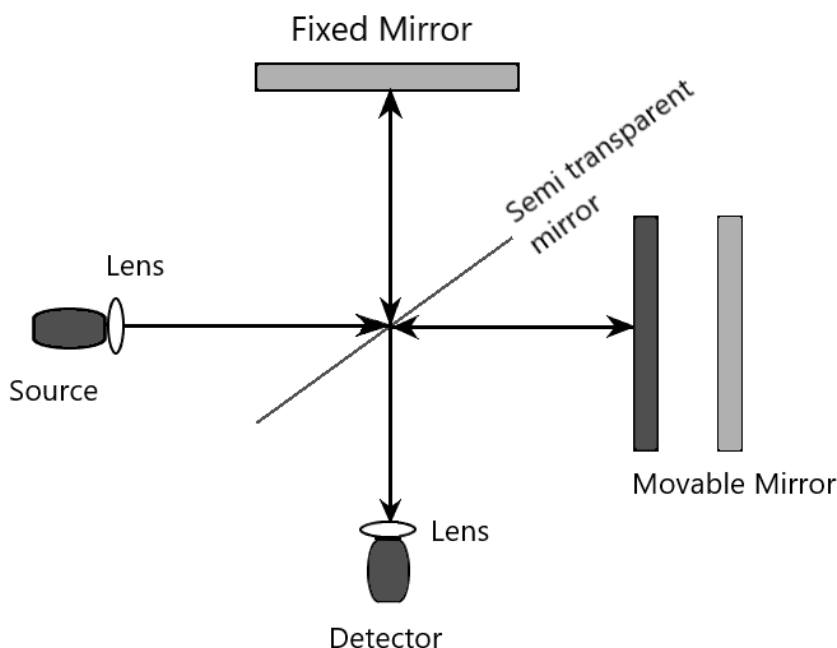


Figure 3: Schematic of FTIR principle

The setup in these experiment consists of a Bruker Alpha FTIR spectrometer coupled with OPUS software to retrieve the data. The spectrometer was fitted with different modules depending on the type of sample. The transmission module was used for liquid and gas analysis by using separate sample holders. The liquid phase could also be analysed both in transmission and attenuated total reflection (ATR) by interchanging with an ATR module.

3.1.1 Absorbance

The absorption phenomena takes place when the frequency of vibrating molecules match the frequency of infrared radiation. When the molecule has matches its frequency in the IR region, its state of energy changes and the excitation of the molecule takes place. This transition in energy states gives rise to characteristic absorption bands. This absorption bands are specific and represent presence of molecules or part of molecules. The evidence for different groups are by infrared absorption and the corresponding bands due to absorption. The instrument is a single beam, hence the beam from the interferometer needs to record the background first and then on the sample of interest. The beam absorption by the sample takes place within the wave number region where the vibration is matched. The analyses for the samples in different phases can be carried out using this principle. Symmetric stretchings or bendings that do not modify the dipole moment of the molecule will not be detected in IR spectroscopy.

For preliminary FTIR experimental gas setup testing, ethanol gas was chosen as sample. The gas cell with diameter 19mm and length 70mm with potassium bromide (KBr) windows, purge was and fixed to the FTIR Spectroscope. An external pump with flux-meter was used for the purging. Based on the series of spectra obtained for the ethanol gas the parameters such as sample scan time, resolution was varied and decided values for resolution was 2 cm^{-1} with a single sample scan time of 4 seconds. These parameters were selected to obtain the fastest response time for the given instrumentation. With these parameters set, the sampling was started to obtain several spectras. The ethanol gas was diffused into the cell. The purging of ethanol gas was done using external pump with lesser flux initially. From the spectrum obtained, it was observed that the decay of the presence of ethanol was slower because, some ethanol was not completely purged. Several spectra were obtained to investigate whether the flux is efficient in purging but the trend remained. To reduce the dead volume of the cell, the volume of the cell was modified.



Figure 4: Modifications made to the FTIR gas cell

The diameter was reduced by placing a cylindrical body inside the cell as shown in figure 4. Smaller holes were drilled to the modified cylinder body. The experiment was repeated with reduced flux to observe whether the purging could be done completely. The results were better compared to the earlier experimental results without the modifications. The purging time became inferior to the time interval between each spectrum due to immediate purging. In addition, the spectra obtained with the trial having maximum flux of the pump were more convincing due to a neater plot compared to the plot without modification with lower flux. The purging was much faster and efficient. Hence it was decided to fix the experiment for full flux of the external pump used for purging. The instrument and measurement cell were set for the fastest response. The drawback was the reduction in intensity of the signals of the sensor almost by half and consequently limiting the sensitivity threshold of the measurement.

3.1.2 Attenuated total reflection [ATR]

This principle of spectroscopy is suitable for the measurements of spectra for the entire infrared region. This procedure does not require complex preparation or pre-treatment of the sample as long as there is good contact with crystal. The instrument measures the internally reflected (total reflection) IR beam when it comes to contact with the sample. This IR beam is incident on an optically dense crystal such as germanium in our case. This crystal has high refractive index at a particular angle. So, it is possible to obtain absorption information of the order of microns of depth from the crystal/material interface. High accuracy is achieved with fourier transform and using appropriate number of scans and resolution. The attenuated IR beam reflected inside the crystal after reflection exits to the detector. The detector reveals the interferogram of the IR beam and the spectrum is generated. The working principle of ATR is described in figure 5

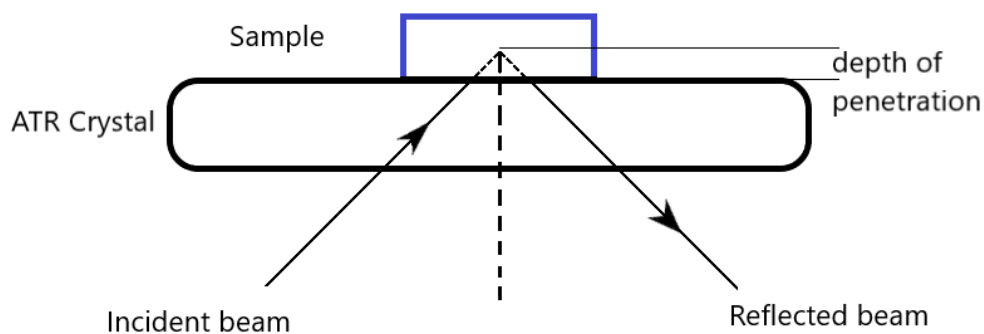


Figure 5: Principle of attenuated total reflection

3.2 Impedance Spectroscopy and Cycling

The positive electrode or cathode is subjected to continuous stress due to higher voltage and oxidation of the electrolyte at a higher rate. As the electrolyte contain lithium salts, this could lead to formation of solid electrolyte interface on the surface of the electrode. This hinders the efficiency and reduces the overall lifetime of the cell by increasing the impedance of the materials up to certain limits. The longevity of cells and loss of energy densities remain a major concern in the long run through the lifetime of the battery. In addition the electrolyte and other components, for example polymer separator layer used can influence the loading of the cell. The porosity of the electrode layers can influence the electrochemical reactions [17], inturn influencing the power/energy densities of the cell.

The impedance spectroscopy used involves a study of eventual changes in the behaviour of dielectric materials in solid or liquid phase in the tested battery cells. The electrochemical impedance spectroscopy involves analysis of materials with ionic conductivity such as solid and liquid electrolytes [18]. The experimental setup for impedance spectroscopy/frequency response analyzer (FRA) measurement was used, as described in figure 6. In the measurement, a set of frequencies of low oscillating current or voltage is applied, the dephasing of current from voltage and its intensity will give the real and imaginary points in the Nyquist. This relation between real and imaginary part of the impedance from the plot is denoted by a semi circle and an eventual increase after the end of semi-circle for the low frequency part of the spectrum.

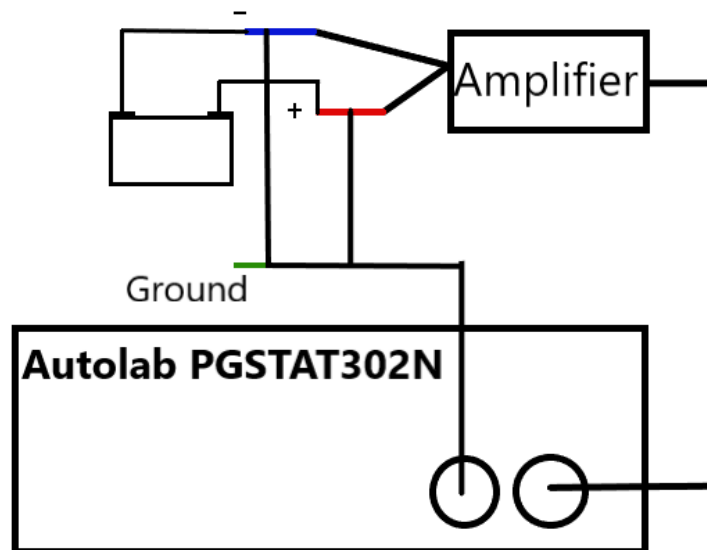


Figure 6: Schematic of FRA measurement.

The charge and discharge cycling of the cells is done within the prescribed voltage limits using a setup consisting of a potentiostat manufactured by Metrohm and the model used is Autolab PGSTAT302N having a maximum current of 2 A and an extended unit; current booster with a range of 20 A at the higher limit as shown in figure 8. To run the experiments and set the suitable parameters, Nova 1.11 software coupled with the metrohm system is used. The extent of change in some of the properties can be studied with the help of impedance spectroscopy to study the variations in the form of complex impedance. The booster was connected to the setup for cell cycling at desired voltage and current limits.

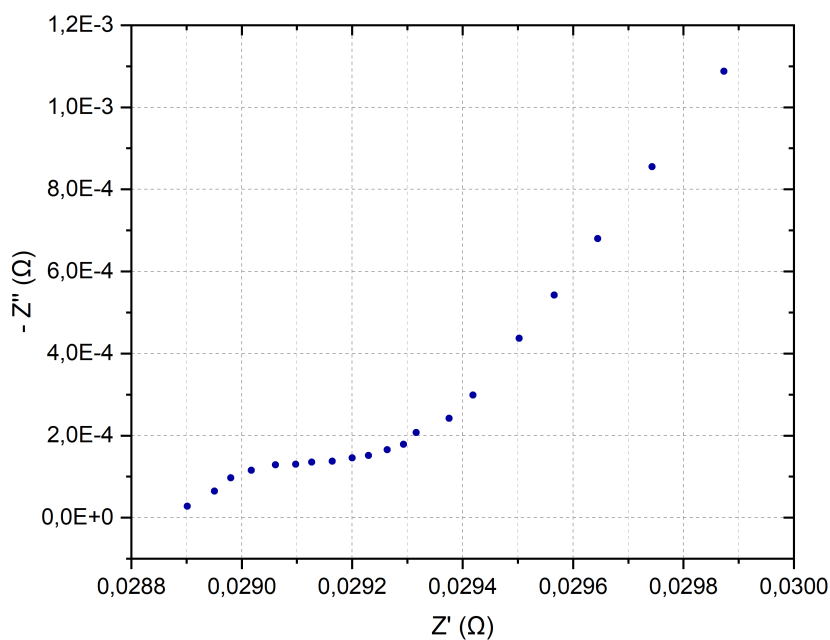


Figure 7: Nyquist plot obtained from test cell 1

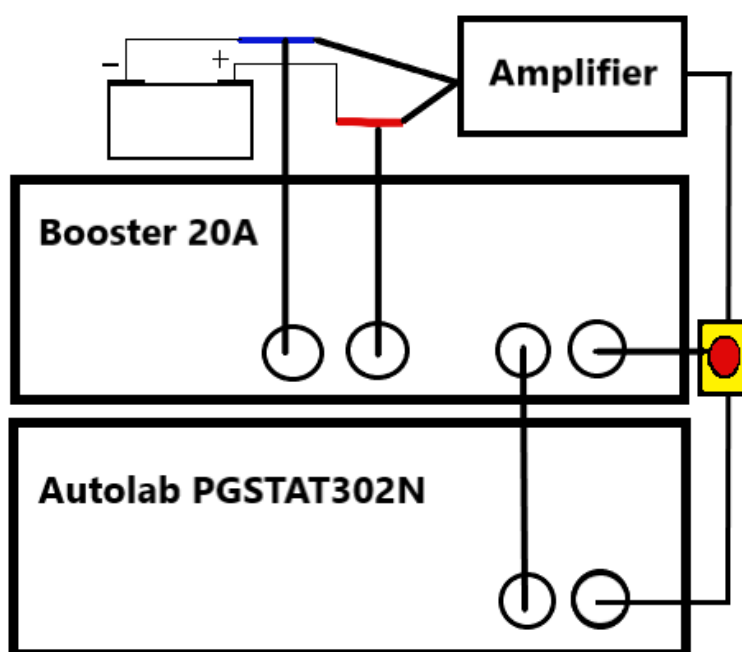


Figure 8: Schematic of setup for cell cycling.

3.3 Thermal Analysis

The experimental setup for thermal analysis involves differential scanning calorimetry (DSC) instruments, Mettler DSC 30 coupled with a liquid nitrogen cooled unit to reach lower temperature of -110°C and a DSC 1 equipment with a lower temperature limit of -70°C and having faster acquisition rate. In these instruments, there is arrangement of reference and sample in a purged chamber as shown in figure 9 and different components are mentioned in table 2 with respect to figure 9. The sample is weighed precisely inside a sealed crucible and placed in the chamber. The temperature controller reads the difference in temperature between the reference and sample and data is gathered in the Mettler software. The analysis can be carried out for both heating or cooling. The behaviour of the sample at various temperatures can be studied. The software calculates the virtual energy required to maintain the temperature equal between reference and sample, shows endothermic or exothermic features as well as changes in heat capacity. The glass transition and phase transition is denoted from the plot of temperature v/s heat flow.

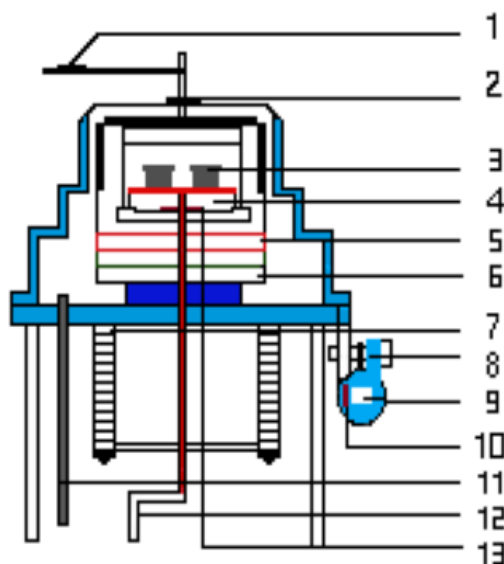


Figure 9: Section of DSC measuring cell.

| Number | Description |
|--------|--------------------------------------|
| 1 | Heat Shield |
| 2 | Automatic furnace lid |
| 3 | Crucible on DSC sensor |
| 4 | Silver furnace |
| 5 | Heater between insulating disks |
| 6 | Thermal resistance for cooler |
| 7 | Compression ring |
| 8 | Cooling flange |
| 9 | Cold finger |
| 10 | Temperature sensor of cooling flange |
| 11 | Dry gas inlet |
| 12 | Purge gas inlet |
| 13 | Temperature sensor of furnace |

Table 2: Parts of the DSC cell

3.4 X-Ray Diffraction

In this method the materials are identified differently from their crystal structures [19] and solid state materials are classified as mono-crystalline, poly-crystalline and amorphous based on their internal atom arrangement [20]. The nature of most of the solid materials are upto 95% crystalline in structure [21]. Hence the difference in diffraction angle and intensities of the diffracted rays are used to examine and characterize the arrangement, position and the distance between atomic planes in the crystals [22].

In principle the X-rays are incident on the solid material. The rays become scattered due to the deflection by the inner core electrons revolving around the nucleus of the atom. They are dispersed in various directions and interfere with each other. The interference can be either constructive or destructive based on the type of interaction between the waves [23]. The diffraction phenomena is the constructive interference of the scattered X-rays. The X-ray diffraction (XRD) is used to analyse the electrode materials in this study. There is a specific XRD pattern for the constituents of each unknown material [24]. This also corresponds to specific set of relative peak positions due to specific inter-planar spacing which serves as a fingerprint to the crystalline structure.

Figure 10 shows the working principle of the XRD apparatus which is based on the constructive interference of the interaction between incident rays and the sample satisfies Bragg's law:

$$n\lambda = 2d \sin \theta \quad (1)$$

where (n) is an integer (λ) is the wavelength of the X-rays and (d) is interplanar distance of diffraction generation and (θ) is the angle of diffraction. The detection and processing of diffracted rays takes place and, all the feasible directions of diffracted rays from sample are obtained by scanning through 2θ angles [25].

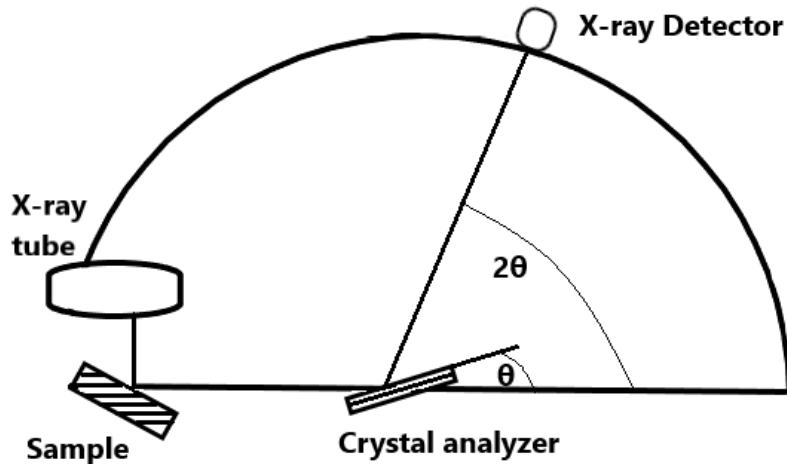


Figure 10: Schematic of X-ray diffractor.

In the Olympus BTX used in this experiments, ultrasonically and dynamically randomised powder was used for collecting the signal with a fixed charged couple device (CCD) camera with 250 acquisitions.

4 Results and Discussion

This section describes the analysis of the results obtained from various experimental procedures that were involved in the thesis. The thesis results and discussions of all experiments that are mentioned in the earlier section can be interpreted with valid reasons based on different figures that can be seen in the following. This part is further divided into subsections depending on the type of method.

4.1 Electrical Characterisation

The impedance spectroscopy was done in order to ensure there is no variations in terms of internal resistance that could affect the measurements in later stages. Then the cycling tests were performed using Metrohm Autolab potentiostat PGSTAT302N with extended booster having current output upto 20 A coupled with Nova software in which the desired programming was executed. The test cell was clamped to a stand and necessary connections were completed. It was decided to cycle test the cells between the prescribed voltage limits between 2.7 V and the upper limit of 4.2 V. The charging cycle was performed with 20 A current till the desired upper voltage limit of 4.2 V and continued with a potentiostatic stage down to a lower current limit of 8 A. Also, discharging cycle at -20 A till the lower voltage limit 2.7 V is attained. The cycle was repeated 25 times for the test cell to observe any minor physical changes. A minor capacity fade of about 5% is observed from the figure 11.

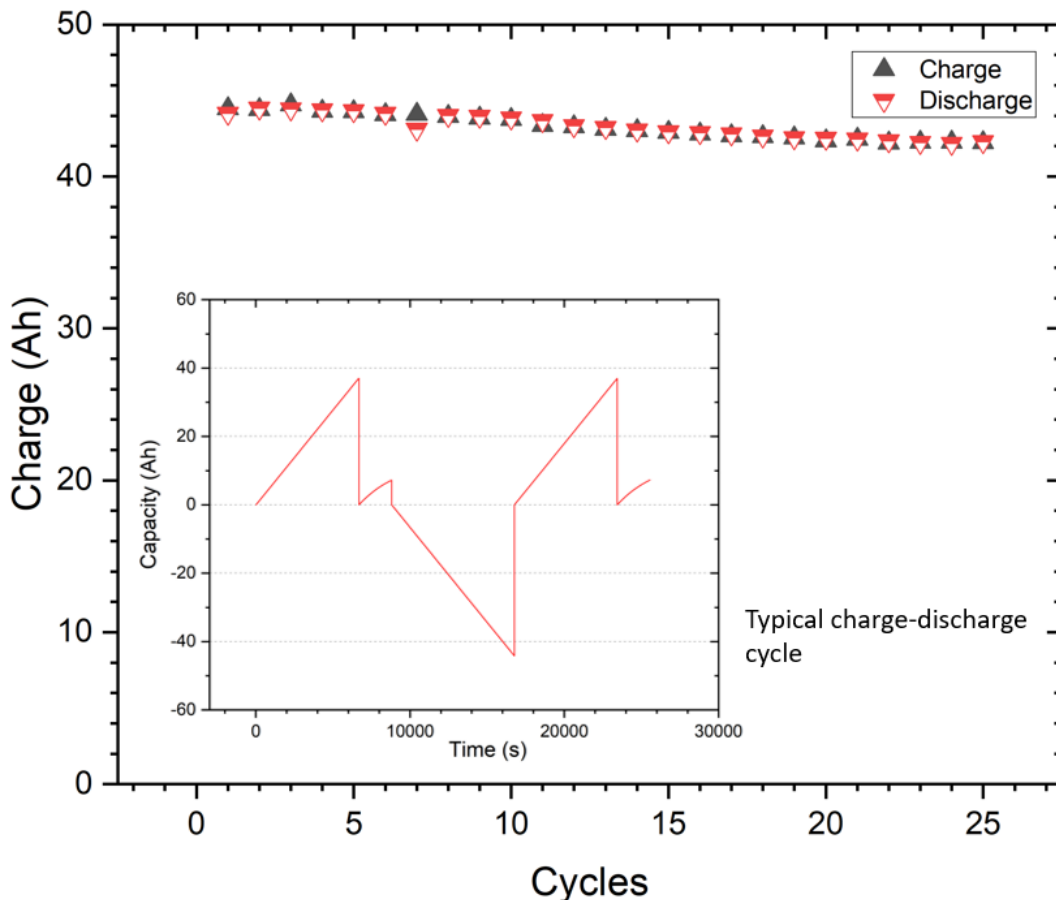


Figure 11: Comparison of charging and discharging cycle for test cell 1.

4.2 Characterisation of battery materials

4.2.1 Dismantling of the test cells

The cells considered for this work are high energy lithium-ion cells having prismatic cell design as mentioned in section 1.1. Since the battery cells were of high capacities, there was a need to completely discharge them to zero volts before dismantling. The cells were measured using precise measuring equipment for weight and clamped to a stand thereby terminals were connected with insulated copper wires for the external connection. The discharge was started using a basic experimental setup with external varying resistance in series with the battery. In addition a voltmeter and a current measuring device was included in the circuit to continuously monitor the voltage and current. The resistance was varied to make sure the current was under safe levels and the discharge was continued until the cell voltage reached 0 V. For dismantling, the cells were placed in an fume hood with safety vents and protective equipment.

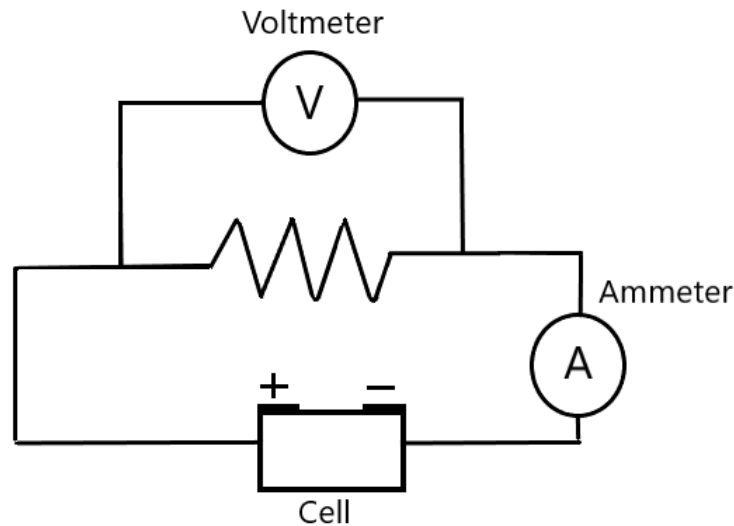


Figure 12: Schematic for cell discharge.

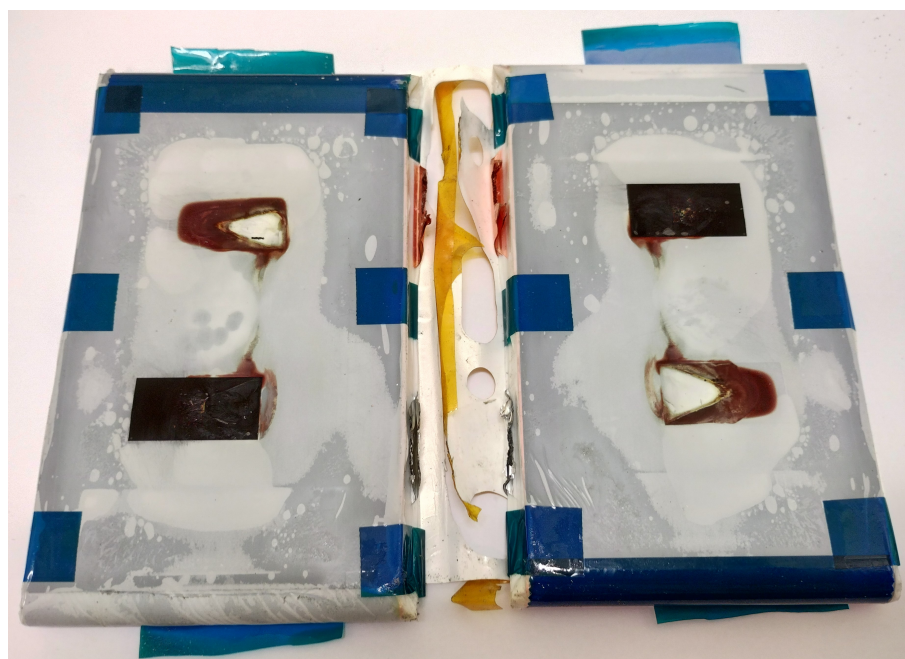
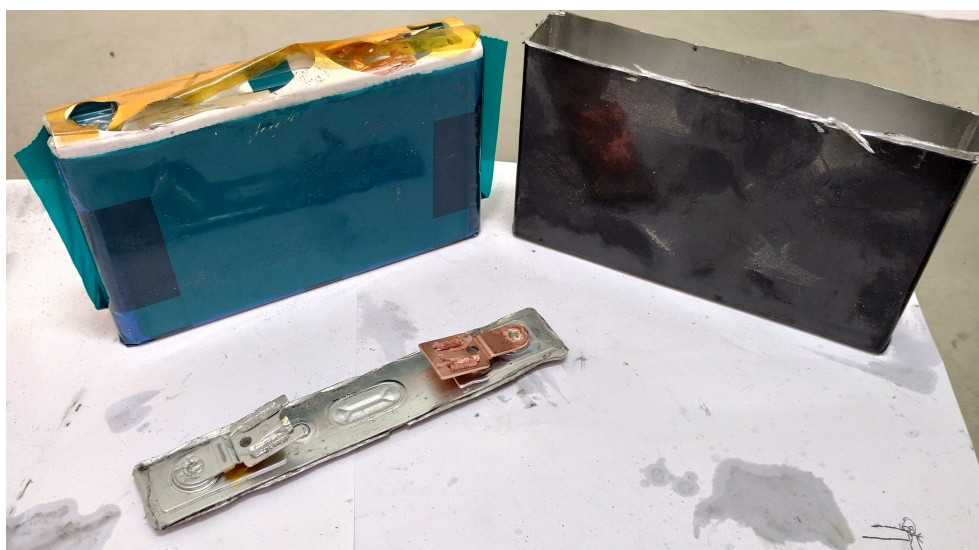
Test Cell - 1 is the first battery cell considered for dismantling was with nominal capacity of 50Ah. The measured voltage before discharging was 3.47 V. The intact battery (see figure 13a) weighed 851.71 grams. The current for discharge was set in a lower range for discharge with varying resistance. Once the cell was completely discharged, the casing was cut open carefully from the top with the assistance of a driller as show in figure 13b. The cell contained two pouches folded horizontally with the copper and aluminium contacts on the upper side. The arrangement of separator and electrode was in separator | electrode | separator | electrode fashion and the combination had a number of horizontal foldings. Also, about 4ml of electrolyte was poured from the case once opened.

Figure 13: Test Cell 1

(a) Intact Test cell 1.



(b) Test Cell 1 dismantled.



(c) Interior packaging of Test cell 1.

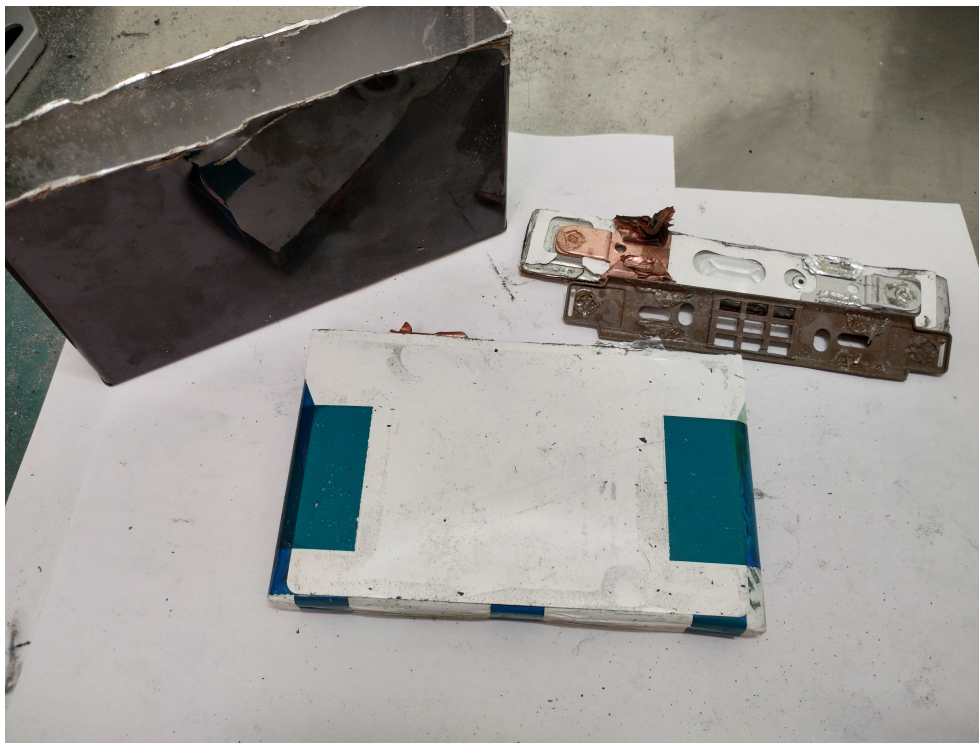
Test Cell - 2 is similar to the test cell one but with a lesser capacity of 37Ah. The test cell 2, also was opened in a similar fashion. The measured voltage before discharging was 3.63 V. The packaging and arrangement was comparable to the test cell 1 as it can be seen from figures 14a and 14b. It also consisted of two pouches folded horizontally with contacts on the upper side as from figure 14c. The arrangement of separator and electrode was in separator| electrode | separator| electrode fashion and the combination had a number of horizontal foldings reported in 1. There was also a small amount of electrolyte.

Figure 14: Test Cell 2

(a) Intact Test cell 2.



(b) Test cell 2 dismantled.





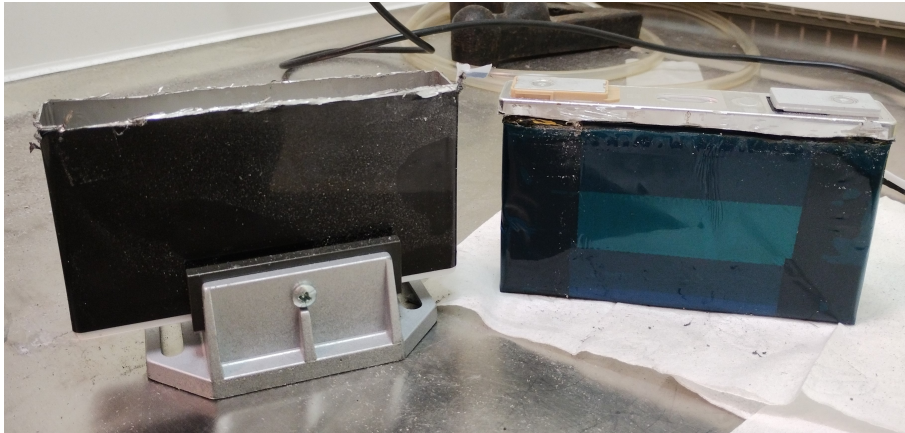
(c) Test Cell 2 interior packaging.

Test Cell - 3 had the least nominal capacity of 20Ah and was also dismantled alike as shown in 15a and 15b. The arrangement of components was slightly different with respect to figures 15c and 15d. The folding of the pouches were made in vertical direction with copper and aluminium contacts on the extreme ends (refer figure 15e). The arrangement of electrodes was as separator | electrode | separator | electrode but folded vertically. Also, a small amount of free electrolyte was present.

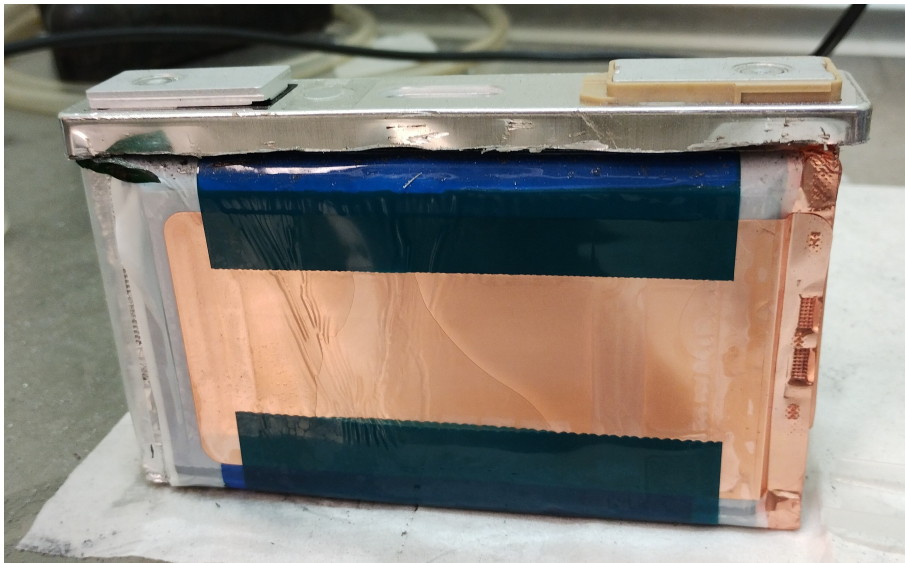
Figure 15: Test Cell 3

(a) Intact Test cell 3





(b) Test Cell 3 dismantled.



(c) Interior components of cell 3.



(d) Packaging of test cell 3



(e) Unpacked test cell 3

The approximate dimensions of interior components are comprehensively mentioned in table 3.

| Parameters | Test cell 1 | Test cell 2 | Test cell 3 |
|-----------------------------------|--------------|--------------|--------------|
| Capacity (Ah) | 49.5 | 37 | 28 |
| Voltage limits(V) | 2.8-4.25 | 2.8-4.2 | 2.8-4.2 |
| Weight (g) | 851.71 | 780.02 | 746.01 |
| Length of Copper electrode (m) | 5.25 x 2 | 5.2 x 2 | 3.8 x 2 |
| Length of Aluminium electrode (m) | 5.2 x 2 | 5.15 x 2 | 3.8 x 2 |
| Width of Copper electrode (m) | 0.08 | 0.08 | 0.12 |
| Width of Aluminium electrode (m) | 0.77 | 0.77 | 0.118 |
| Length of Separators (m) | 12 x 2 | 12 x 2 | 8 x 2 |
| No.of foldings | 39 x 2 | 39 x 2 | 49 x 2 |
| Area (m ²) | 0.42 x 2 x 2 | 0.42 x 2 x 2 | 0.41 x 2 x 2 |

Table 3: Approximate dimensions of cell packaging

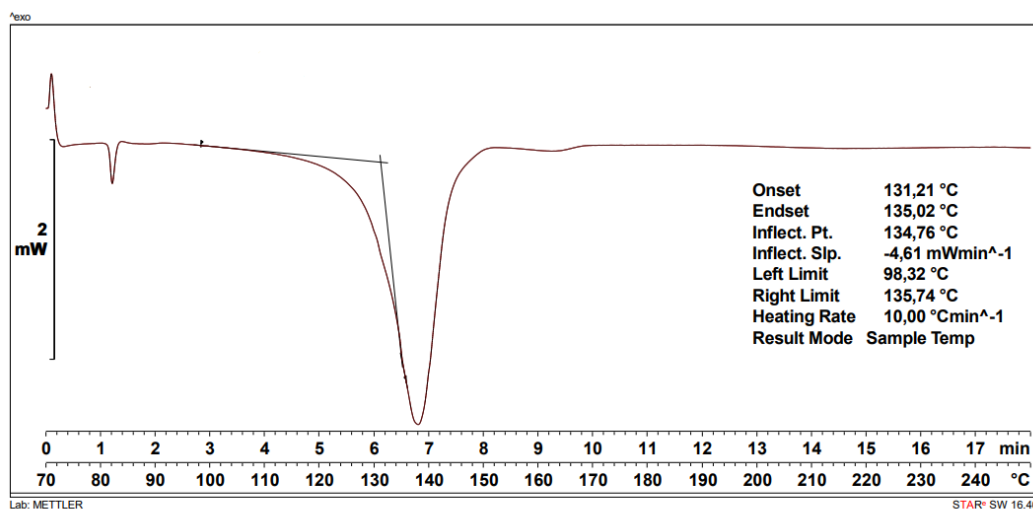
4.2.2 Thermal Analysis [DSC]

The separator was extracted from the test cell 1 and three trials were conducted under DSC analysis. First the separator was tested directly after extraction. In some samples there was an exothermic peak around 70°C because of some contaminant. This might be due to unwashed electrolyte. The onset of the melting peak was around 135°C. In the second trial the sample was just wiped with a clean paper without using any cleaning agents. The exothermic peak reappeared but it was small. In further trials separator sample was thoroughly cleaned with ethanol and tested again with the experiment set to run twice. This time the plot was more neat and it was observed that the melting point is at about 135°C, also the exothermic peak disappeared. For that reason, it was decided to clean with ethanol for the other separators.

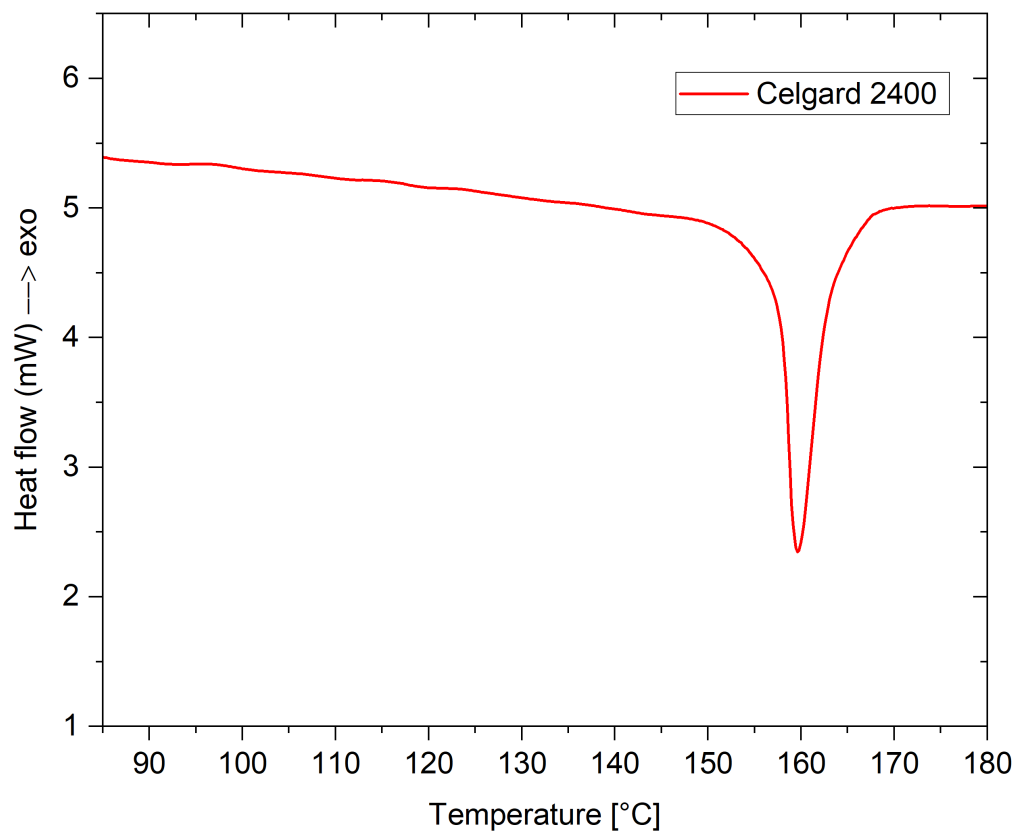
As the principle and procedures are explained in detail in the experiments section, the separator from all the test cells was extracted and was cleaned thoroughly with ethanol to free from electrolyte impurities and dust particles. The separator weight was measured precisely and was placed in the DSC instrument. The DSC curve for a separator is shown in 16a. The heating rate 10°C/min was used for all the samples.

Figure 16: Heat flow curves of separators.

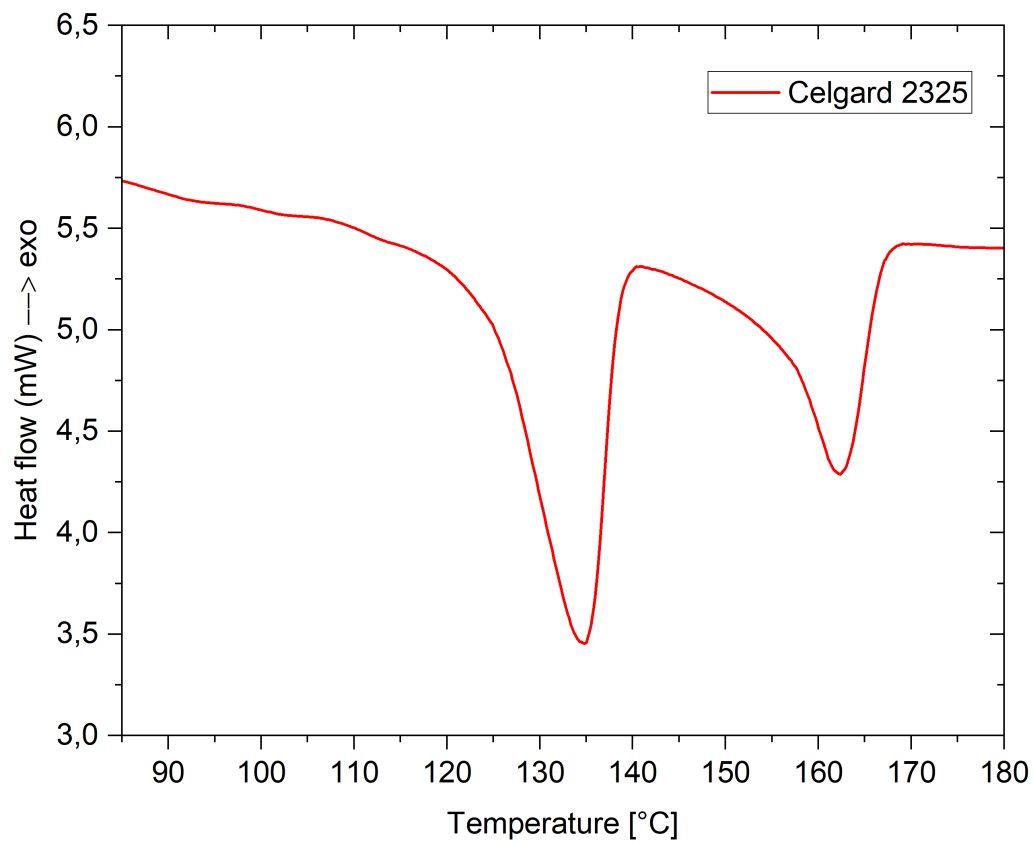
(a) General heat flow curve for separators measured in DSC experiment.



In order to determine the type and material of the separator, two additional fresh separators manufactured by Celgard were used for comparison. The different characteristics of these separators can be seen from 16b and 16c. For further analysis, while the major component of the peak had onset at 135°C, the peak appears to be asymmetric into a spot at lower onset temperature.



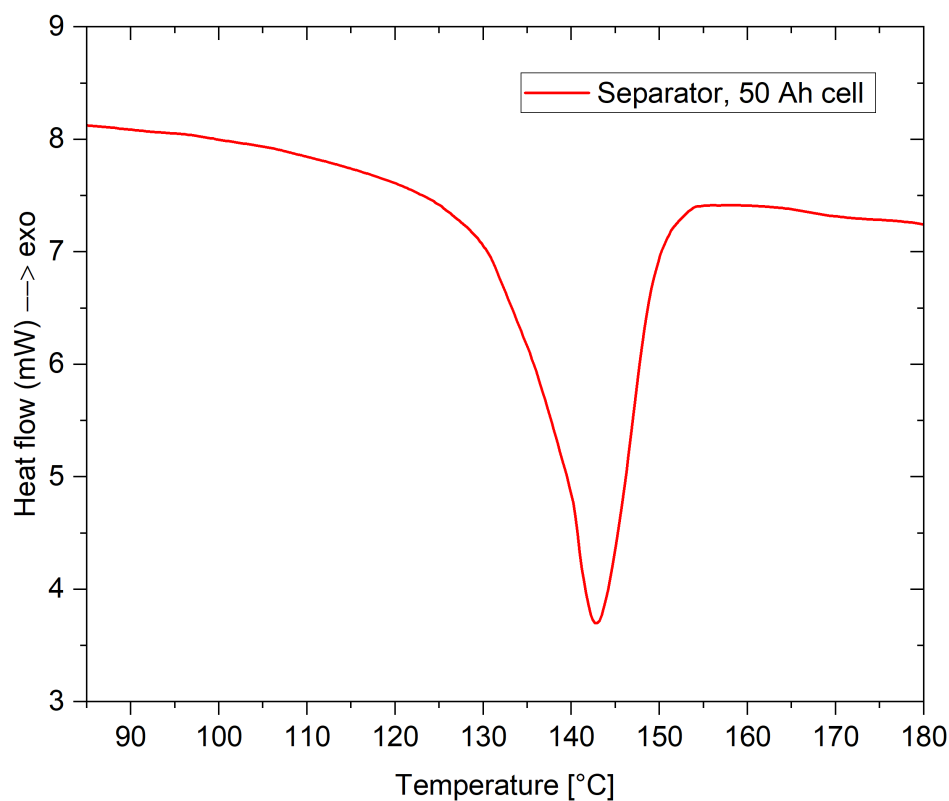
(b) Heat flow curve of Celgard 2400 separator taken from DSC30 instrument.



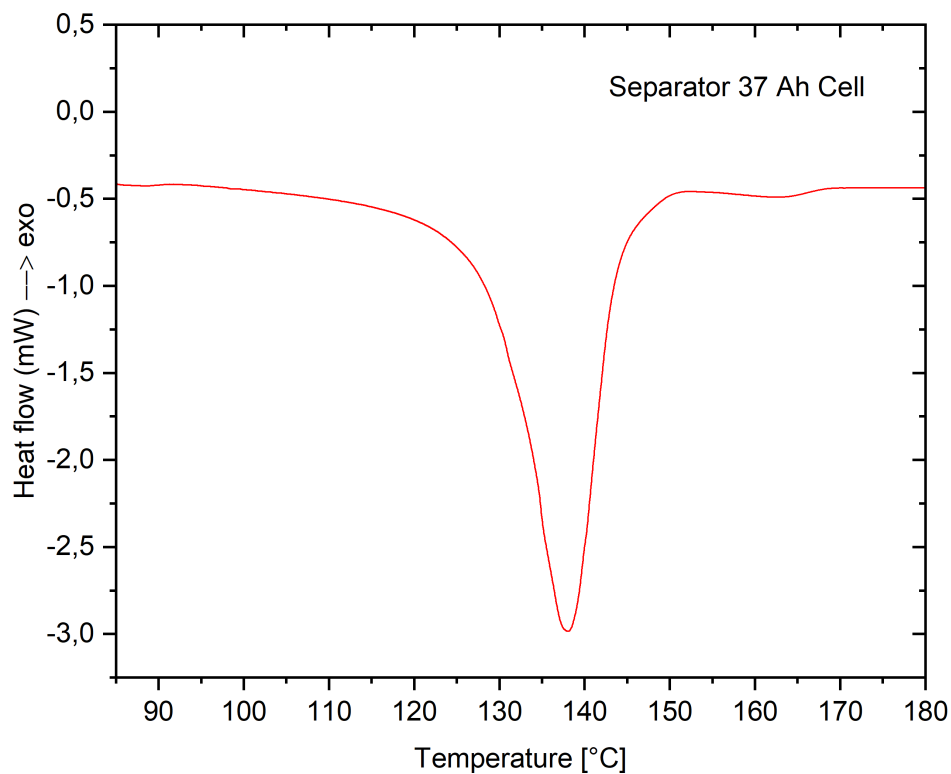
(c) Heat flow curve of Celgard 2325 separator taken from DSC30 instrument.

The first separator model specification was Celgard 2400. The heat flow vs temperature curve observed from figure16b, denotes that the onset temperature is around 150°C. However, the composition of this separator was given by the manufacturer, it was a single material made from polypropylene (PP). The second separator was specified as Celgard 2325 seen figure16c. The heat flow curve shows that the composition has two different onset temperatures, one at 125° and other close to 150°C. Hence, the separator is composed of two different materials. The exact composition was triple layered (PP/PE/PE), polyethylene (PE) sandwiched between two polypropylene (PP) layers.

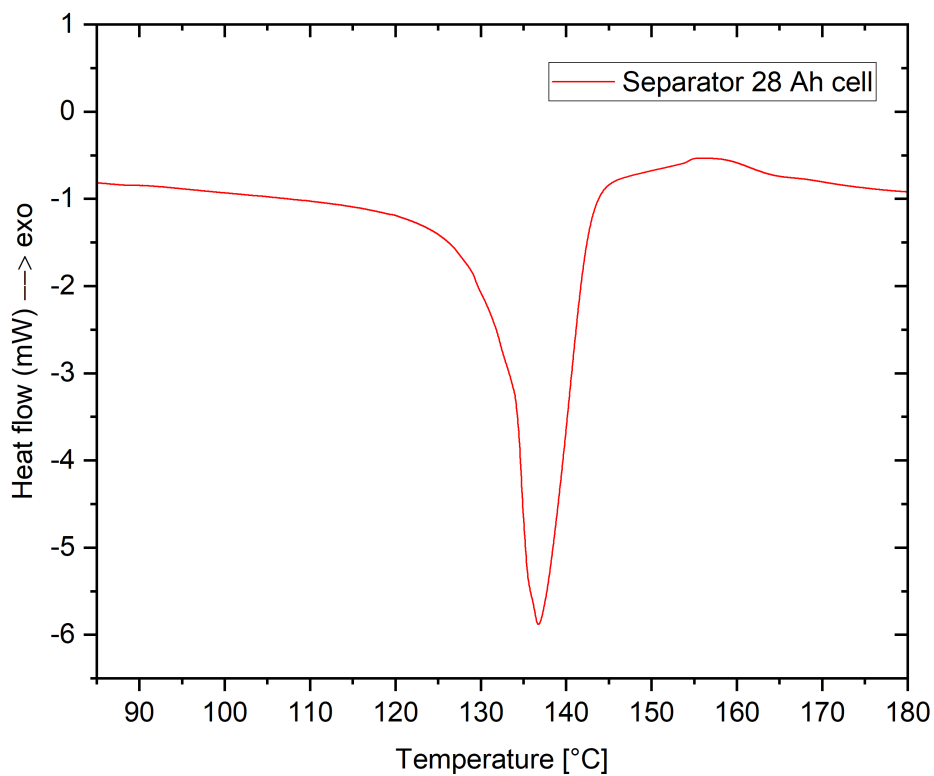
The figures (d,e,f) represents the heat flow curves of the separators from the test cell 1, test cell 2 and test cell 3 respectively. In figure d it is observed that the onset temperature is around 126°C with a peak at about 140°C. The same inference can be obtained for test cell 2 and test cell 3 from figures (e and f) respectively. Hence the inference is made that the separator composition of all the test cells was single layered made of only one type of material.



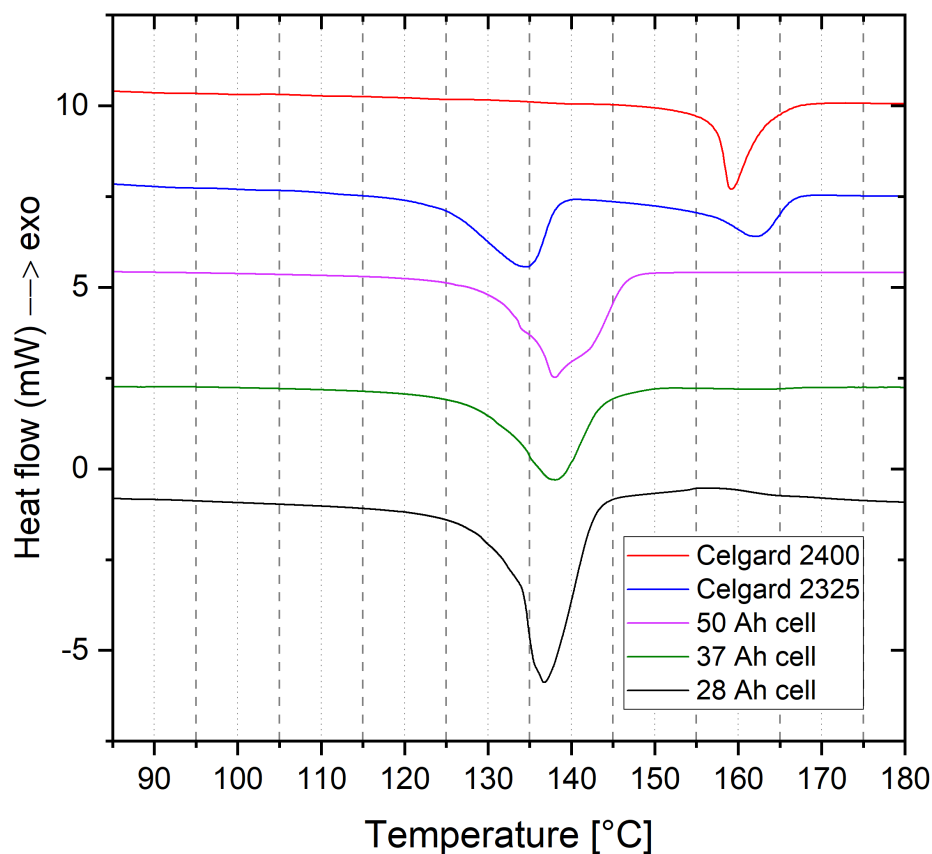
(d) Heat flow curve of Test cell 1 separator taken from DSC1 instrument.



(e) Heat flow curve of Test cell 2 separator taken from DSC1 instrument.



(f) Heat flow curve of Test cell 3 separator taken from DSC1 instrument.



(g) Comparison of all the separators for onset temperatures at heating rate of $10^{\circ}\text{C}/\text{min}$

It is observed that the peaks from all three test cells from figures d,e and f is at about 140°C with onset temperature about 126°C , which corresponds to the first peak in figure c. Therefore, the separator material is similar to the PE layer from celgard 2325. Hence it can be concluded that the separator in all the test cells could be made from single layer polyethylene (PE). The figure 16g and table 4 gives the detailed information about this.

| Separator | Onset Temperature ($^{\circ}\text{C}$) |
|--------------|--|
| Test cell 1 | 126.1 |
| Test cell 2 | 125.9 |
| Test cell 3 | 126.6 |
| Celgard 2400 | 155.5 |
| Celgard 2325 | 125.81 and 155.1 |

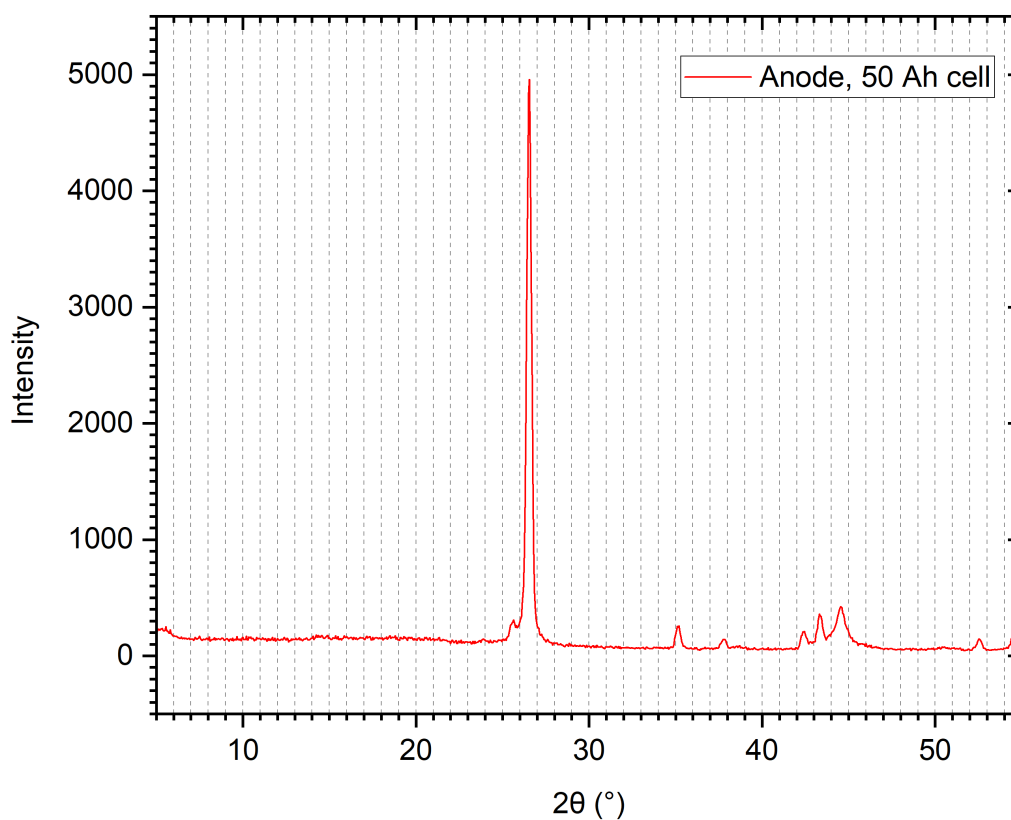
Table 4: Onset temperatures of separator samples

4.2.3 X-ray Diffraction [XRD]

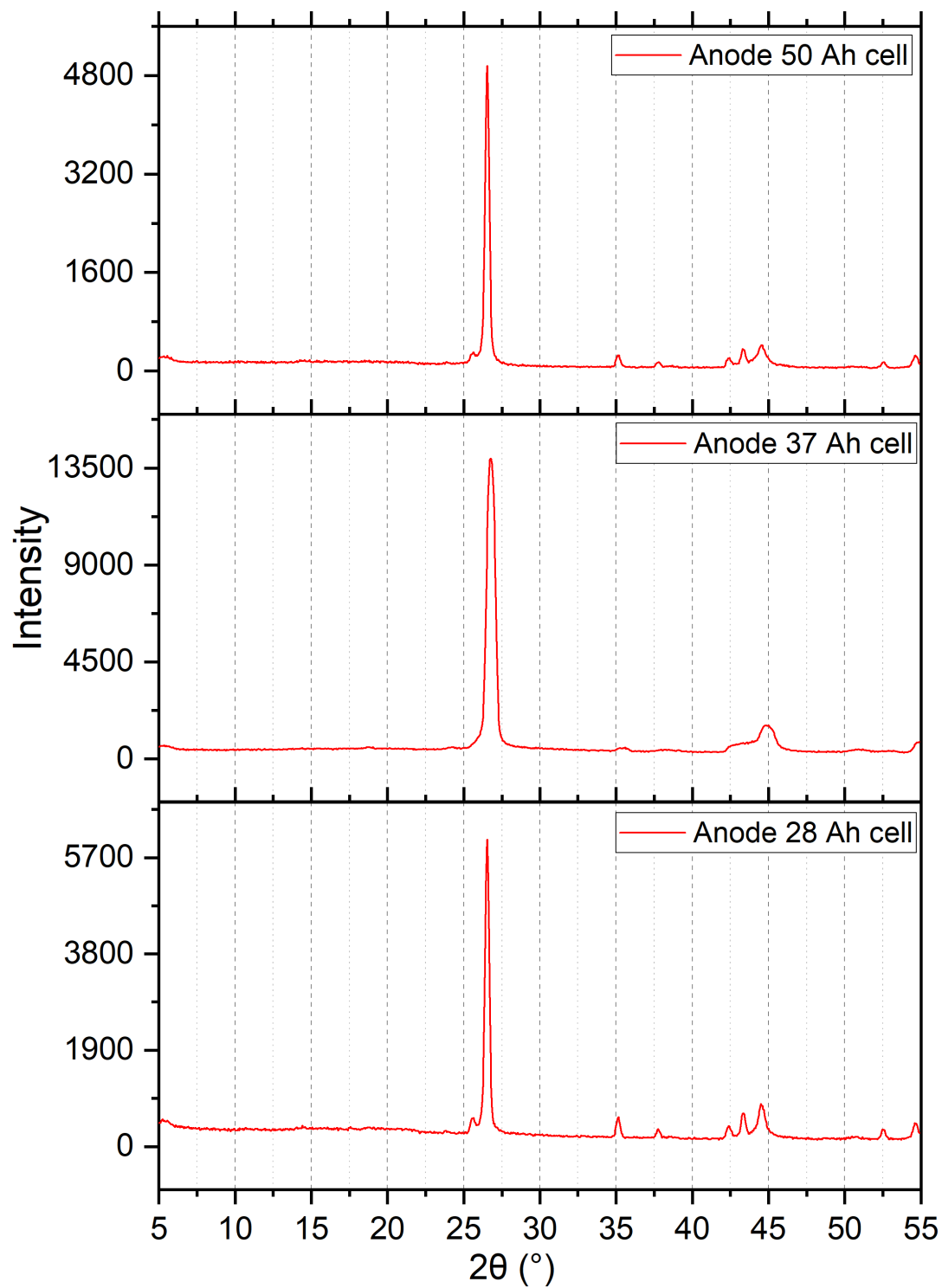
This characterisation method involves extracting powder material from both cathode and anode of the test cells to interpret the different compositions. The analysis is done with the X-ray diffraction instrument as described in the earlier section. The extraction of material from the electrode involve simple procedures like scraping of the materials from the electrode of dismantled. Then the scraped powder is crushed finely and shaken manually with the help of a sieve to reach the desired size of particles as described by the instrument specifications. In addition, the powder was also dried for about thirty minutes at 200°C to get rid of any moisture and solvent.

Figure 17: Electrode Material X-ray Diffraction Patterns

(a) Diffraction pattern of Test cell 1 - anode material

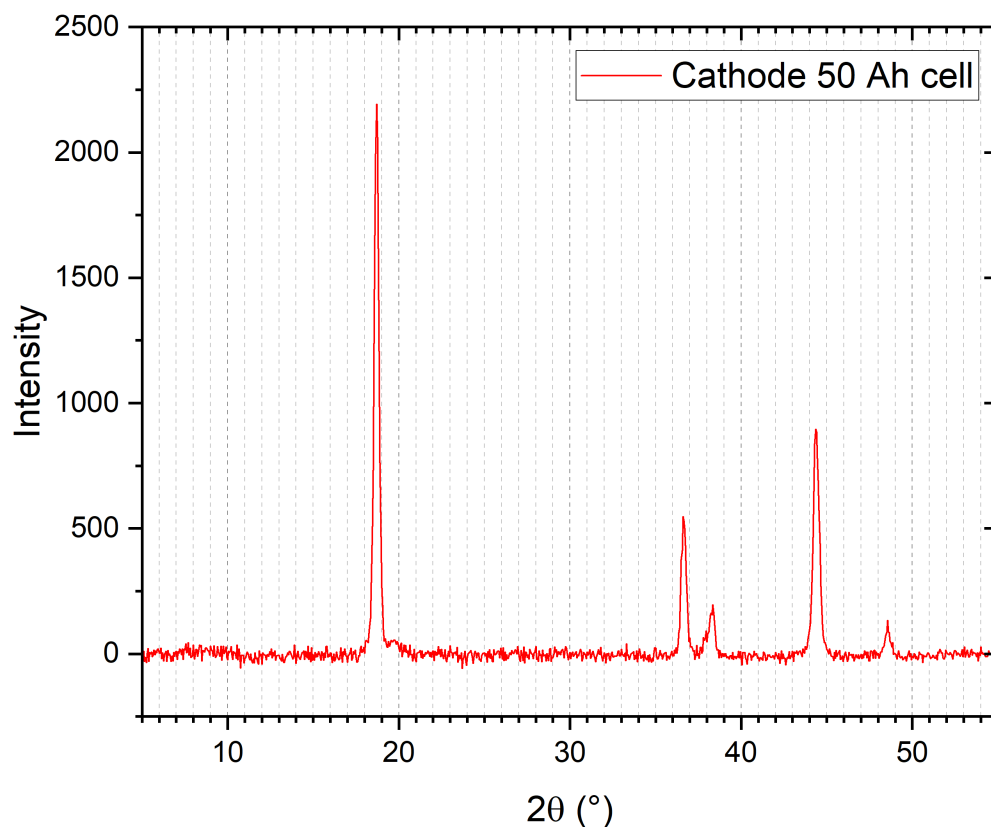


The obtained X-ray Diffraction Patterns (XRD) patterns are analysed based on the type of electrode material in the batteries. Figure 17a and 17b represent the anode material of three test cells. The peaks observed at 2θ 26.4° correspond to those of graphite in the composition. Also, the small peaks at 54.5° and 44.5° in 17a is the additional evidence for graphite [26],[27]. Hence, not surprising it can be said that graphite is the major anode material in the battery cells. In addition, some minor peaks are present for all anode materials tested. The origin of these peaks is yet unknown.



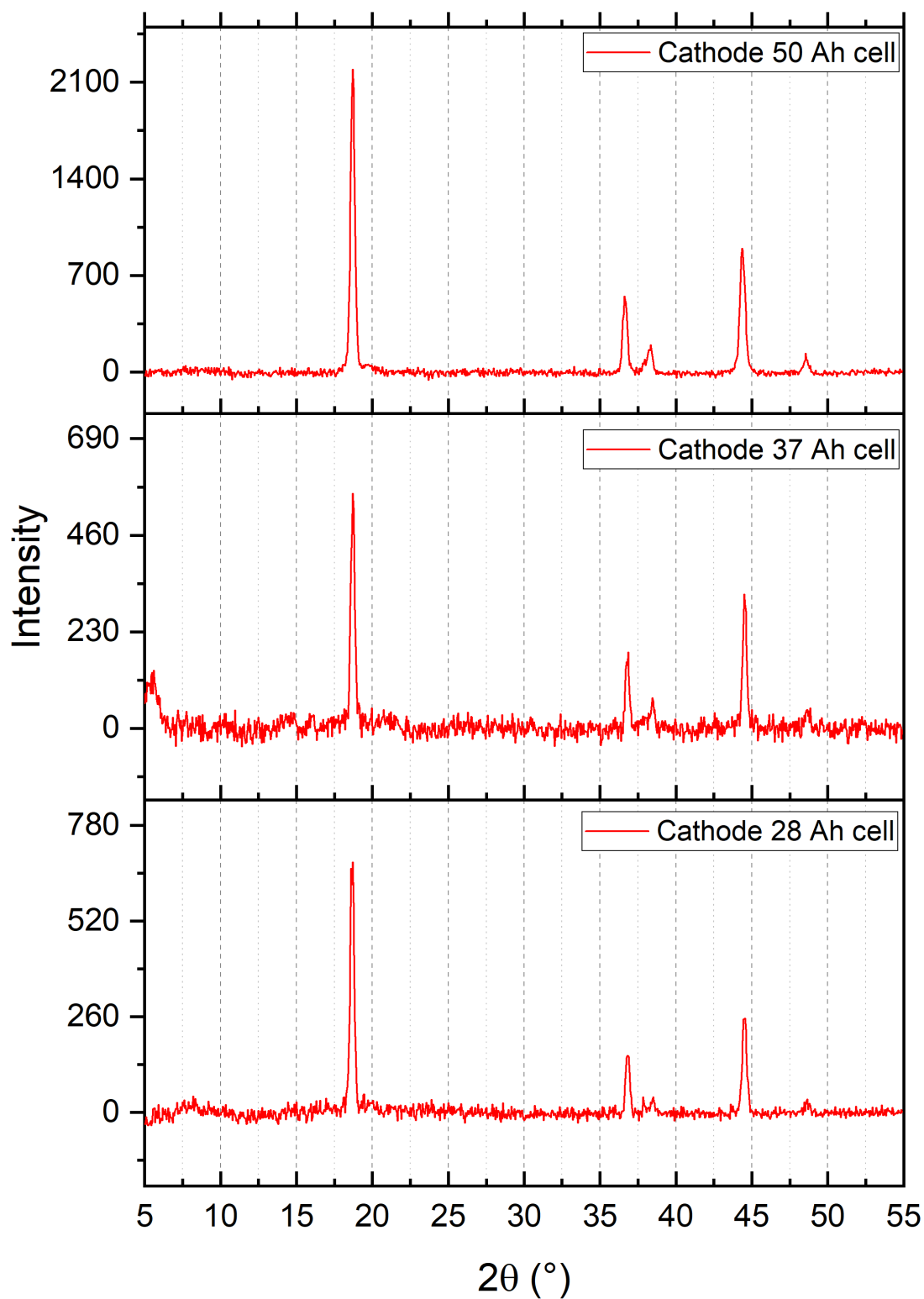
(b) Diffraction pattern of test cell 1, 2 and 3 - anode material

Figures 17c and 17d represent the XRD patterns of the cathode material of the different test cells. The strong peak at $2\theta=19^\circ$ is a characteristic of the pure NMC material [28]. Further, the doublets at 36° and 38° and the isolated peak at about 44.5° as well as the 48.5° are characteristic peaks of pristine NMC material as mentioned in [28]. Hence the cathode material of all the battery cells is composed of NMC without traces of any other material as detected by the X-ray diffractometer.



(c) Diffraction pattern of Test cell 1 - cathode material

In addition, the XRD patterns of anode and cathode materials after extraction, grinding and heating shows no evidence of crystal degradation and contamination. So, the results seem reasonable.



(d) Diffraction pattern of test cell 1, 2 and 3 - cathode material

4.2.4 Fourier Transform Infrared Spectroscopy [FTIR]

The electrolyte sample extracted from the test cell 1 was subjected to study with FTIR spectroscopy (see section 3.1). The electrolyte in most of the today's cells are made of a salt, primarily lithium hexafluorophosphate (LiPF_6) dissolved in combinations of volatile and non volatile organic carbonates. For instance the possible organic compounds could be cyclic nonvolatile carbonates like ethylene carbonate (EC), propylene carbonate (PC) [29] or linear volatile carbonates such as ethyl methyl carbonate (EMC), diethyl carbonate (DEC) and dimethyl carbonate (DMC) and vinyl carbonate (VC). The chemical structures of some of these compounds are mentioned in the section 1.3.2. The aim of this experimental method is to investigate and characterise any deviations from the expected composition that might influence the safety.

The analysis of the electrolyte present in test cell 1 is presented in figure 18 and the most relevant absorption peaks are reported in table 5 and the assignments are suggested. The bands are described as: vs= very strong, s=strong, m=medium, w=weak and vw=very weak depending on the relative intensity.

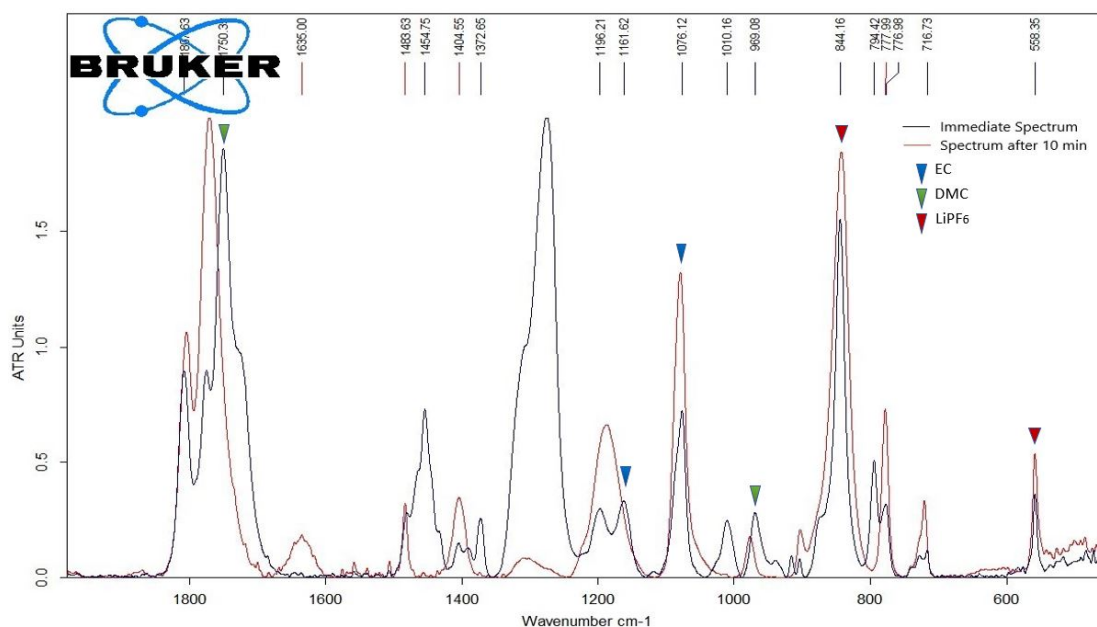


Figure 18: ATR spectrum of liquid electrolyte extracted from test cell 1

From the initial examination the presence of solvents like EC and DMC could be considered according to the assignments mentioned in [15]. In addition the F-P bending and F-P stretching is observed at positions 558 cm^{-1} and 845 cm^{-1} respectively [15]. They correspond to LiPF_6 . The volatile compound DMC evaporates rapidly. Due to this the relative intensity of salt and other solvents, mostly EC, increases over time.

Figure 18 shows the spectrum obtained from the electrolyte extracted from test cell 1 in the region between 2000 cm^{-1} and 500 cm^{-1} . The spectra are baseline corrected and normalized to 2. The volatile DMC disappears over time. This explains the disappearance of the peak after at 1280 cm^{-1} . Also this can be supported with the shift of the peak at 1800 cm^{-1} . The variation of composition due to evaporation shifts the peak from 1750 cm^{-1} to 1807 cm^{-1} , which is a shift of mixture of EC and a volatile organic linear carbonate to the typical frequency of pure EC. From figure 3 in [15] a neat peak at about 1076 cm^{-1} which signifies the strong presence of ethylene carbonate (EC) and also the

| Assignment | Wavenumber (cm ⁻¹) | Measured (cm ⁻¹) |
|---|--------------------------------|------------------------------|
| Vibration frequencies of DMC [30] | | |
| CO ₃ out of plane deformation | 795 m | |
| CH ₃ -O stretching | 915 m | |
| CO ₃ -O stretching | 969 m | 969 |
| O-C-O asymmetric stretching | 1281 vs | 1281 |
| CH ₃ symmetric deformation | 1437 m | |
| CH ₃ asymmetric deformation | 1456 s | 1454 |
| C=O stretching | 1751 vs | 1750 |
| Vibration frequencies of EC [31] | | |
| ring bending | 717 w | |
| perturbated ring bending | 729 w | |
| CH ₂ rocking | 777 m | |
| perturbated CH ₂ rocking | 795 m | |
| ring breathing | 904 w | |
| perturbated ring breathing | 916 w | |
| ring stretching | 971 m | |
| ring stretching | 1077 vs | 1076 |
| ring stretching | 1162 s | 1161 |
| CH ₂ wagging | 1394 w | |
| CH ₂ scissoring | 1483 m | |
| ring breathing | 1776 vs | |
| C=O stretching | 1808 vs | 1807 |
| Vibrational frequencies of LiPF₆ [15] | | |
| F-P bending | 558 vs | 558 |
| F-P stretching | 845 vs | 844 |

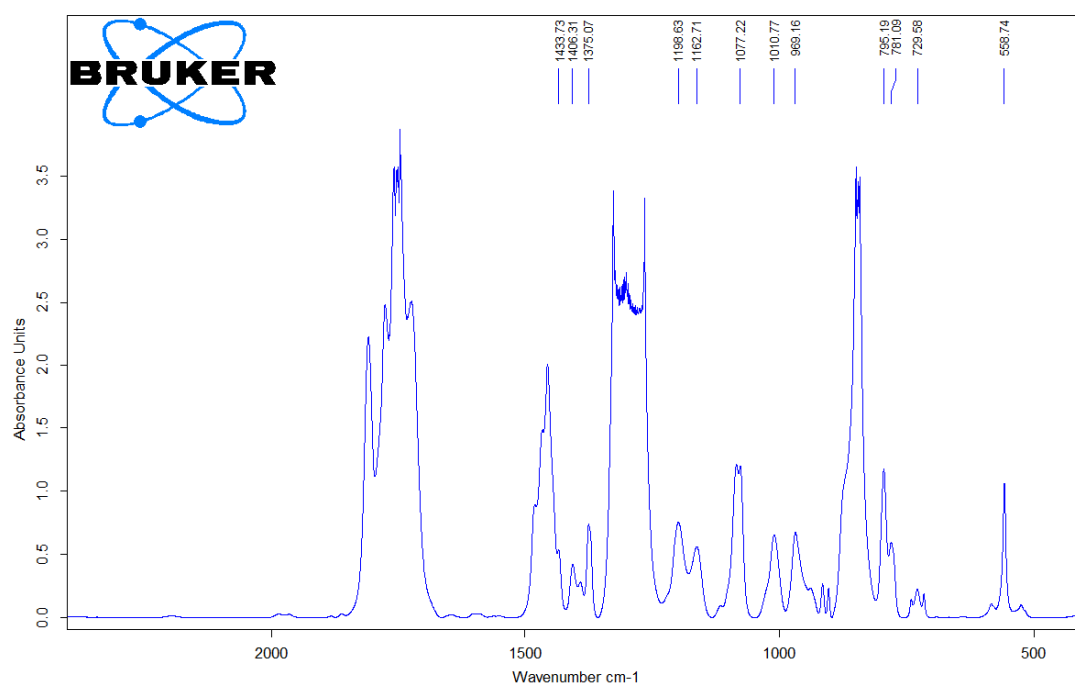
Table 5: Assignments of spectrum bands from ATR spectrum of extracted electrolyte out of test cell 1 at different evaporation time.

absence of propylene carbonate (PC) at that particular position. In addition, the presence of strong peak at 1161 cm⁻¹ in the figure supports the absence of PC, since there is no evidence of any peak for PC at that position from figure 1 a and table 4 in [15]. The peak at 558 cm⁻¹ and 844.1 cm⁻¹ from figure 18 correlates to the mentioned assignments in table 5 for lithium salt. Hence it can be concluded that electrolyte mainly contains a mixture of EC and DMC with lithium salt LiPF₆. Also there is possibility of the presence of other solvents which could be identified through an extended analysis.

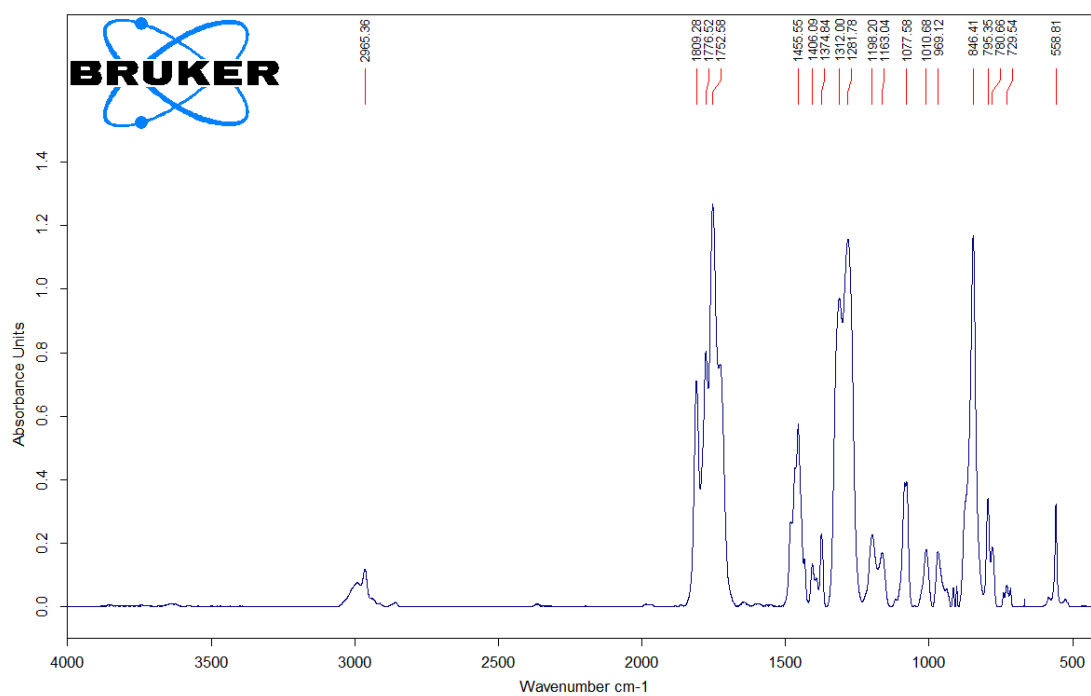
Figure 19a and figure 19b represent the thick and thin sample transmission spectrum respectively taken using a liquid sample holder with two KBr units of 4mm radius, acquired at the time when the test cell 1 was dismantled. It can be observed that the spectrum of the thick sample is less noisy and the larger peaks are saturated. While the smaller peaks of the fingerprint region are well visible. From the thin sample spectrum, peaks are very distinct and all the major peaks position of the DMC, EC and LiPF₆ can be clearly compared to that of corresponding values in table 5 and the corresponding absorbance spectrum as well.

Figure 19: Transmission spectrum of liquid phase electrolyte

(a) Transmission spectrum of thick layer liquid electrolyte extracted from test cell 1.



(b) Transmission spectrum of thin layer liquid electrolyte extracted from test cell 1.



4.3 Abuse testing

The test cell 1 was abuse tested by overcharging beyond the limits of the cell. The test was performed at Alelion Energy Systems outdoor test facility with necessary fire hazard and safety protocols. The test cell was placed in a metallic box without cover with ventilation holes. To induce overcharge, a charger with output upto 100 A was connected in series with the test cell. The overcharge was started at 25 A and increased upto 50 A. The test was repeated for two times with two different battery cells of the same type. In the second cell the venting valve was manually pierced. The different gas sensors for hydrogen fluoride (HF), carbon monoxide (CO), volatile organic compounds (VOC) and methane CH₄ were incorporated in the testing setup to which the gases were fed using different pipes. The pipe to the methane sensor was 6 mm inner diameter and about 4m in length and 2 mm inner diameter and 5 m in length for all other sensors and FTIR. The raw signals from the sensors were collected in the form of voltage. The voltage and ppm ratings are mentioned in the table 6. Also the cell temperature, ambient temperature inside the box and air temperature were continuously measured during the entire course of the tests. The FTIR with gas cell was utilised for gas analysis. The gases were taken from an external pump with flux of 1.5 liter/minute to the analyser. The realtime data for temperature and voltage levels were monitored and logged using an Agilent 34972A Data Acquisition unit. The raw data from the sensors and spectrum from FTIR were analysed and will be interpreted further.

| Gases | HF | VOC | CO | CH ₄ |
|---------------------|------|--------|------|-----------------|
| Voltage levels (V) | 1-5 | 1-5 | 1-5 | 1-5 |
| Gas emissions (ppm) | 0-50 | 0-1000 | 0-75 | 0-18000 |

Table 6: Ratings of the gas sensors

In the first overcharging experiment, the battery cell was placed as it is to observe what happens with overcharging. There was a spontaneous venting followed by violent break of the case and flame. The overcharging current was not interrupted at the start of venting and was continued till start of the flame. The outcome of this test was harsh as the battery opened up violently giving an outburst of gases and materials with complete disintegration of the case. The current was disconnected after the burning. During the successive overcharging experiment, the cell vent was pierced for better collection of the vented gases. This time the outburst of gases was slower due to reduced pressure, the gathered data was much more detailed as there was a wider time gap between venting and the flame. The current supply was interrupted at the start of venting. But still, the cell ignited after some time with complete incineration of all the inner materials due to the flame.

There are some limitations of the abuse test. Firstly, better organisation for gas collection for more representative gas/fumes sampling. Second, the sensing of the IR was focused on promptness instead of higher sensibility. Third, the number of iterations for the experiment was limited. Further, advanced camera for better recording for the course of experiment could have produced finer results.

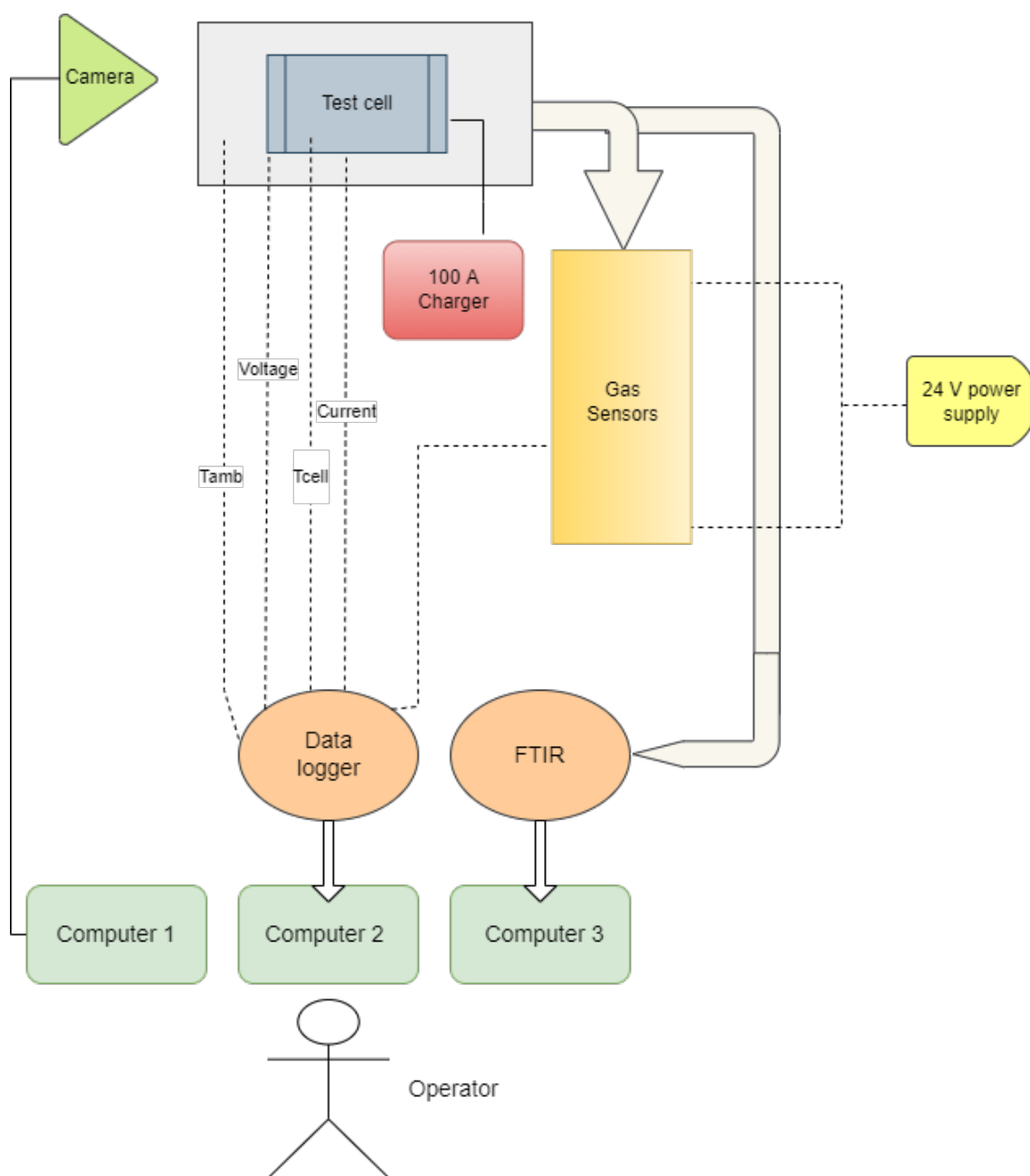


Figure 20: Schematic of the abuse test cite

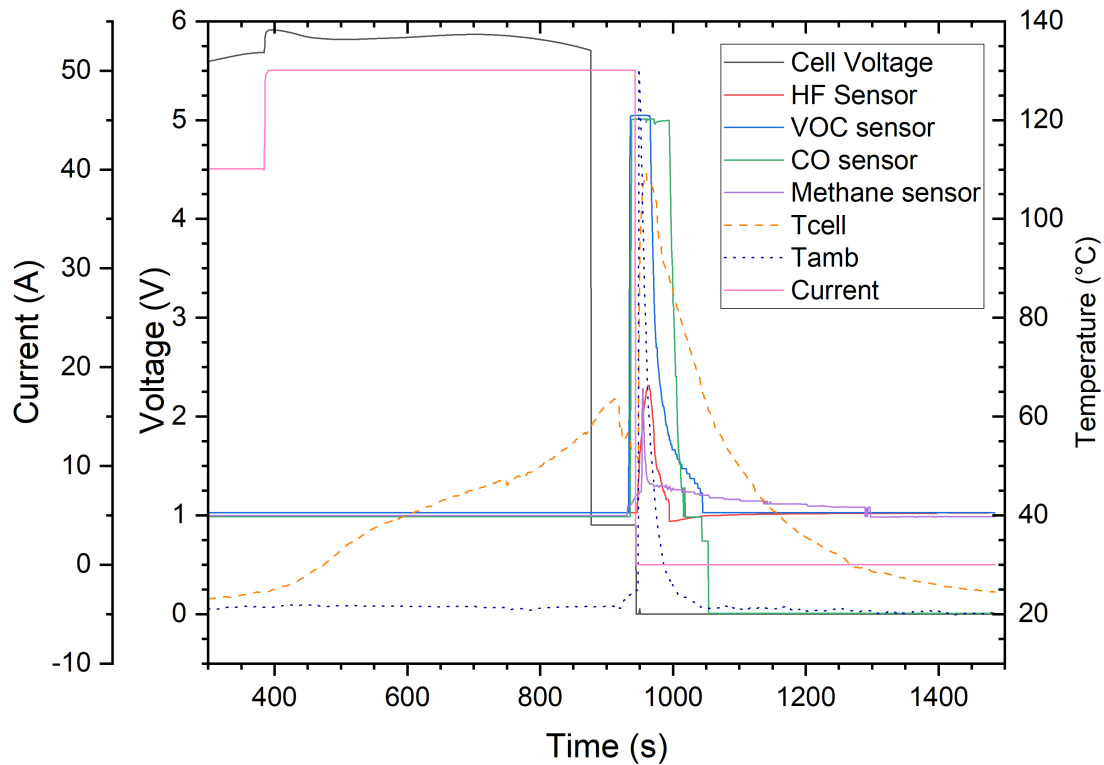
The figure 20 is the schematic of the abuse test cite. The white large arrows represent the piping for gas collection to the sensors and FTIR. The black dotted lines represent the electrical connections from thermocouples and voltage signals to the data logger. A separate 24 V power supply was provided according to the specification of the sensors. Also, camera was fixed near the position of the test cell to monitor the events during the tests. Three separate computers were used, one for camera recording, one for data logger and one for FTIR as shown in the setup. The computers were placed at a safe distance where the operator monitored the events.

4.3.1 Outline of the experiment 1 results

The cell was weighed precisely before the test and was 886.3 grams inclusive of spot welded contacts. The test on cell 1 started with current at 25 A and after 45 minutes it was increased to 50 A. After 1 hour from the overcharging was started, the test was interrupted on day 1 and it was observed that the voltage was 4.47 V and cell was swollen in the centre by almost 5mm. The test was restarted on day 2 with the current at 40 A, it was eventually increased to 50 A. Approximately after 15 minutes venting occurred followed by fire. The results from this event are described in figure 21a of overcharging.

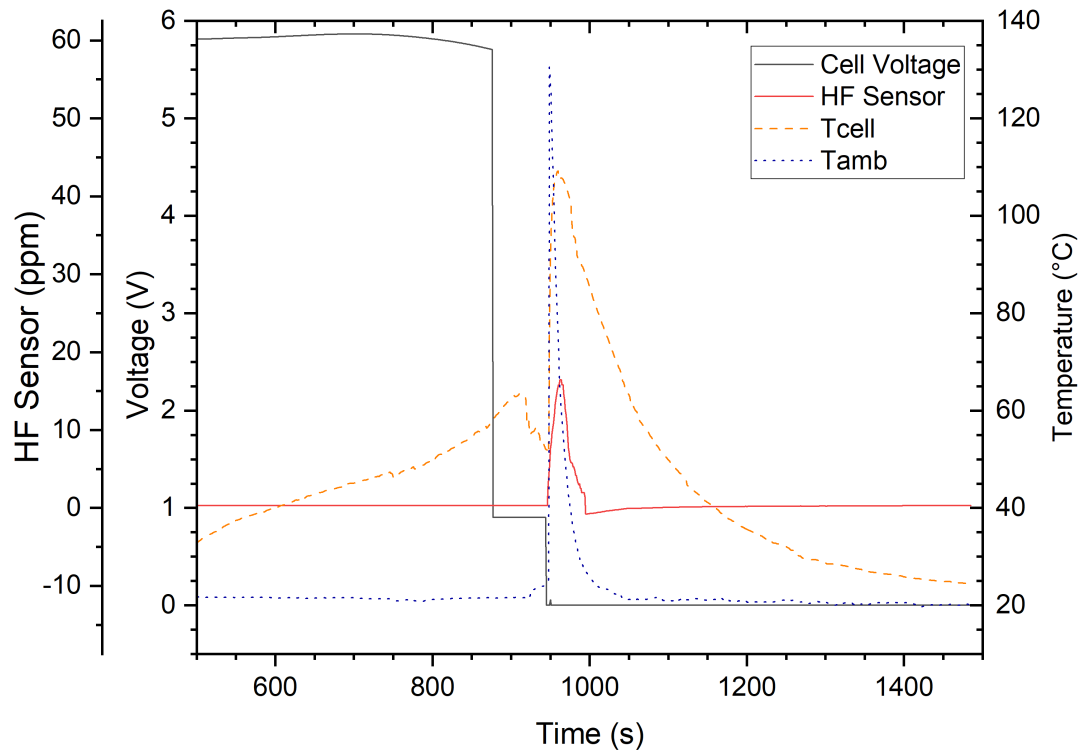
Figure 21: Trace graphs of emissions during the experiment 1

(a) Overall Trace of the overall signals during test



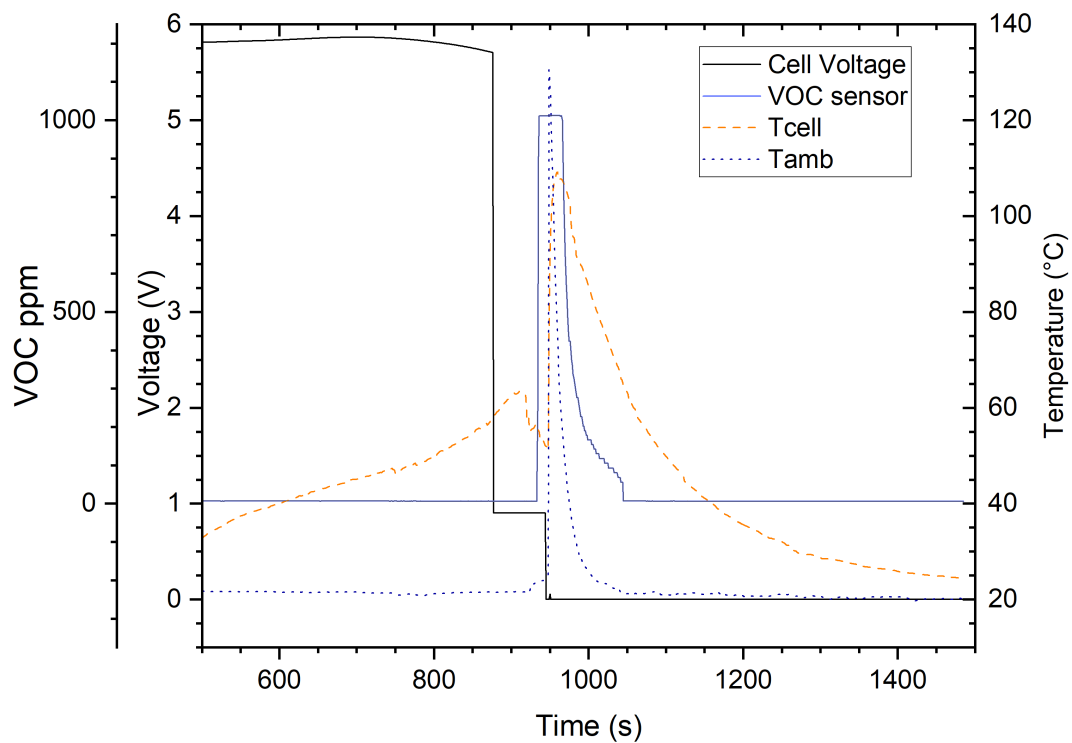
From the trace plot 21a the voltage reaches a maximum limit at 5.8 V and remains fairly stable around that range and gradually decays to 5.65 V, when the current of 50 A is applied constantly. The cell temperature increases steadily up to 58°C with the increase in voltage. After the visible venting the voltage dropped to 1 V. This is possibly the start of failure as the cell temperature reaches 63°C. Then there was sudden venting before the ignition took place with eruption of several gases. The ambient temperature is 109°C at this stage. The gases are emitted collectively and some of them persist for a longer time.

The plot 21b describes the event when the HF gas eruption takes place. The sensor picks the signal exactly when the fire ignites. The ambient and the cell temperature reach their highest values and almost simultaneously as the peak of HF signal is recorded at 2.3 V. It translates up to 12.5 ppm HF when the cell temperature had its maximum.

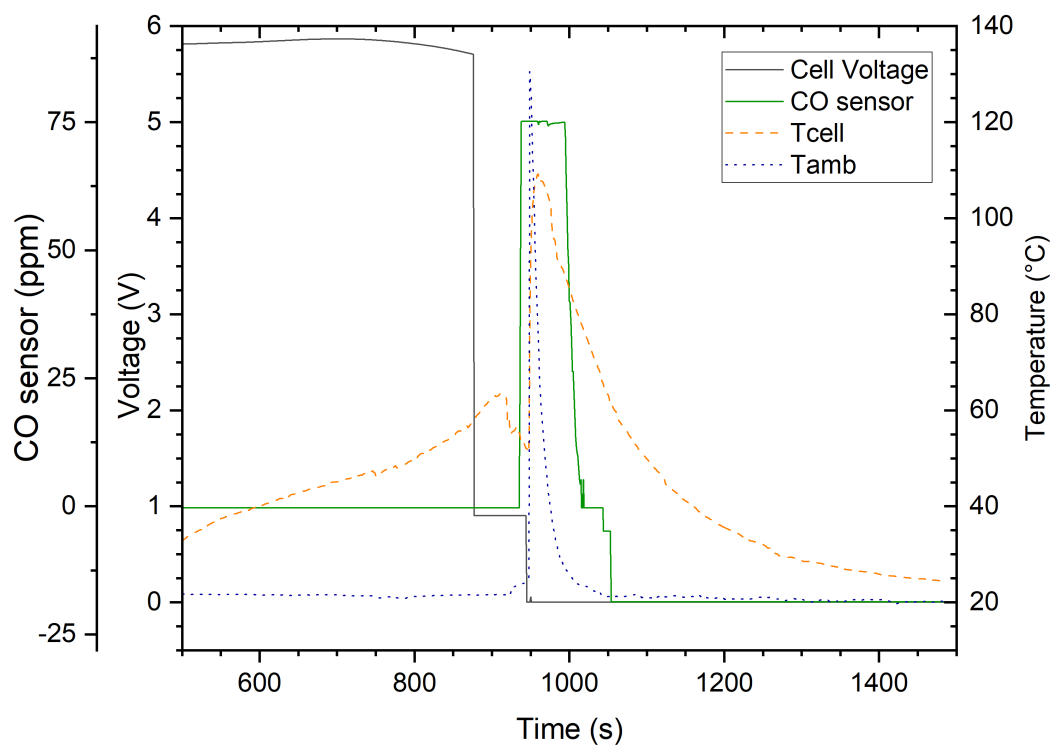


(b) Trace of hydrogen fluoride emission

Further the trace from VOC can be seen in figure 21c which is emitted slightly before the HF. Also the VOC emissions are at full intensity at 5V according to the sensor signal, which match to the 1000 ppm rating.

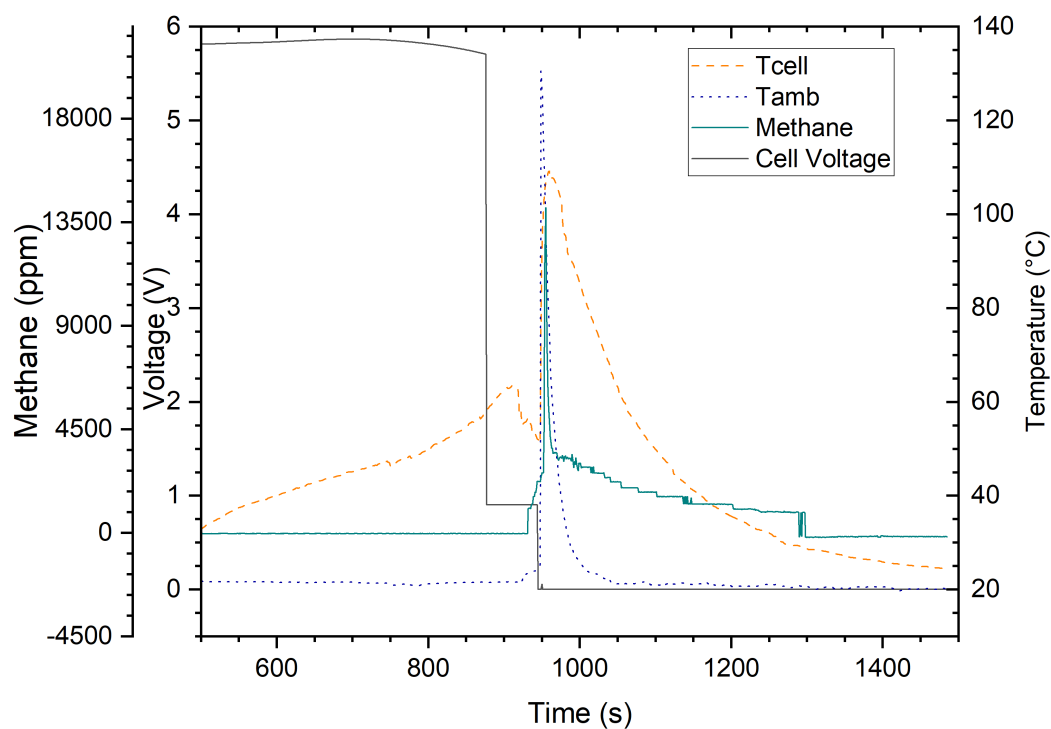


(c) Trace of volatile compounds emission



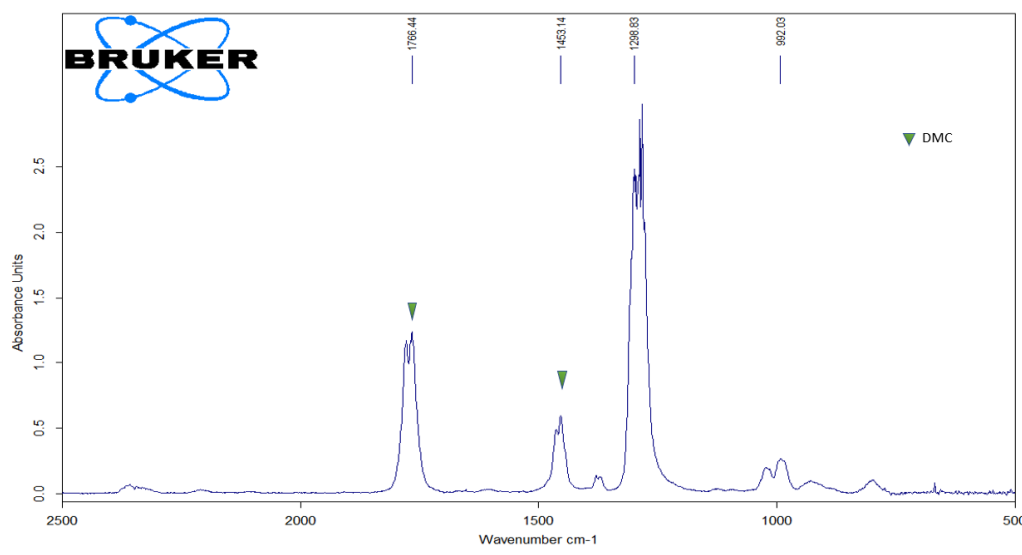
(d) Trace of carbon monoxide emission

The trace plots of CO and CH₄ are shown in 21d and 21e respectively. The plots indicate that the carbon monoxide and methane are emitted mostly at the same time at around 58°C when the voltage drops and reach their peak when the ignition is observed. The CO is measured at over 75 ppm and CH₄ at about 14000 ppm.

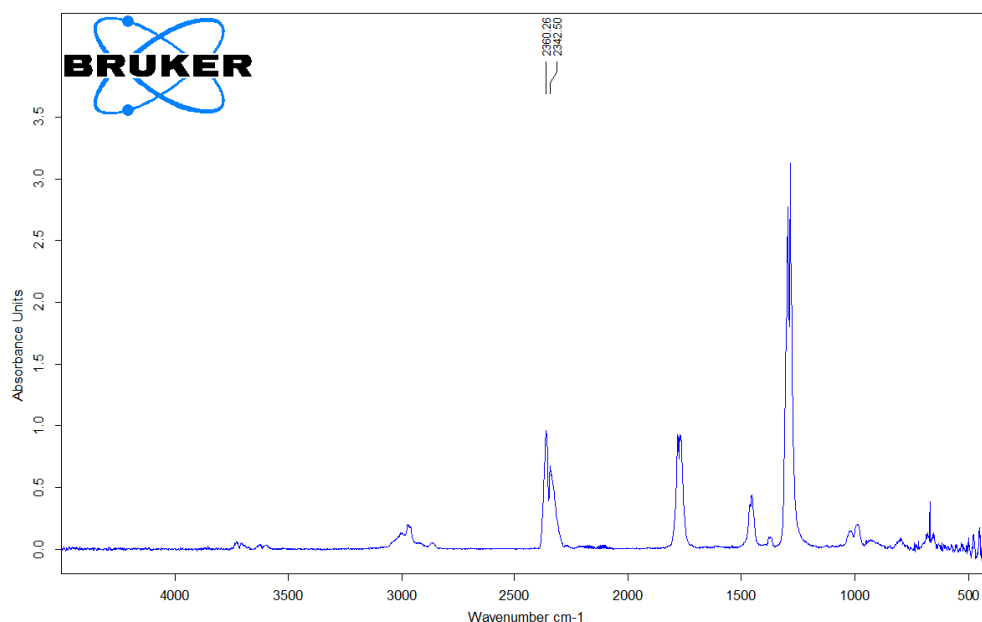


(e) Trace of methane emission

4.3.2 FTIR Spectrum analysis from experiment 1

Figure 22: Gas emission FTIR spectrum from abuse test**(a)** Dimethyl carbonate gas emission spectrum at 957 second

In figure 22a a very strong peaks are observed at 1290 cm⁻¹ and 1766 cm⁻¹ and with smaller peak at 1453 cm⁻¹. This peak is a strong peak in case of pure solvent. Hence all these peaks strongly prove the DMC emissions during venting. Also, very strong peaks at 2342 cm⁻¹ and 2360 cm⁻¹ are observed from the gas emission spectrum. These are the indicative peaks which precisely correlates to the wave-numbers of CO stretching seen in table 7.

**(b)** Carbon dioxide and carbon monoxide gas emission spectrum at 977 second

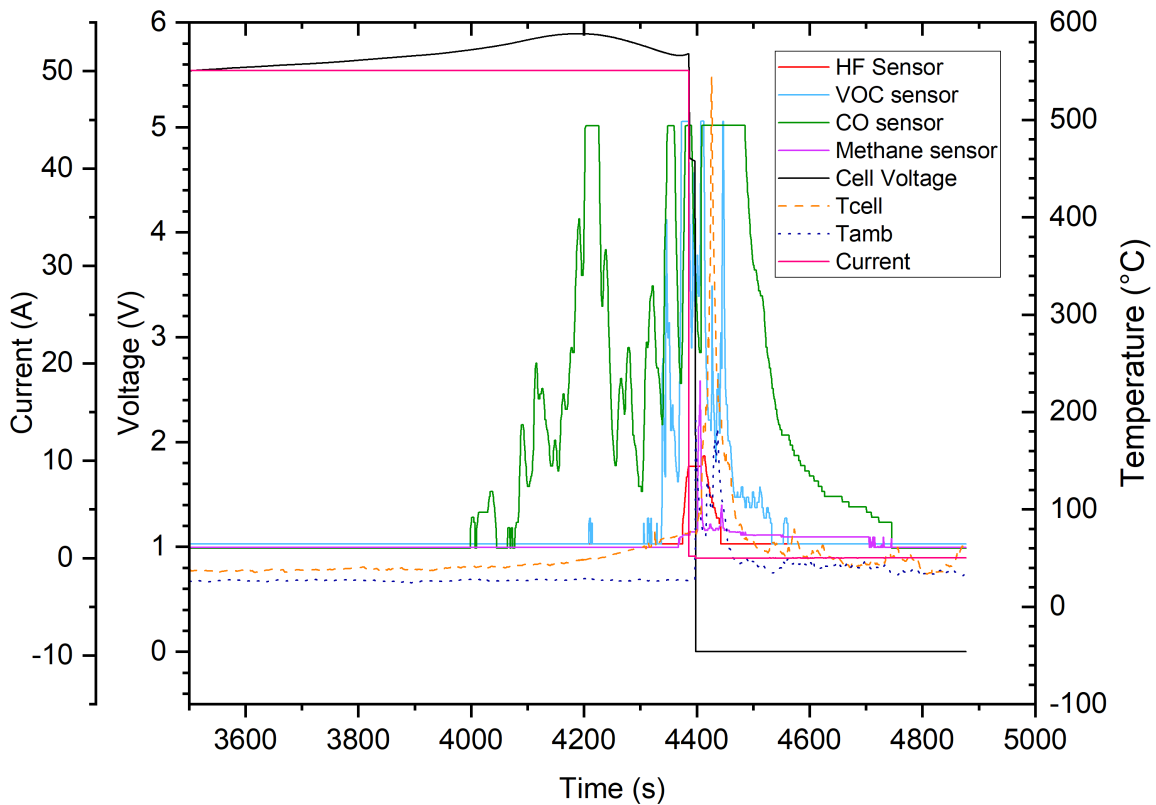
As the venting was sudden, with the given settings of the FTIR instrument it was not possible to observe the trace of hydrogen fluoride in this case. However it was detected by the sensor.

4.3.3 Outline of the experiment 2 results

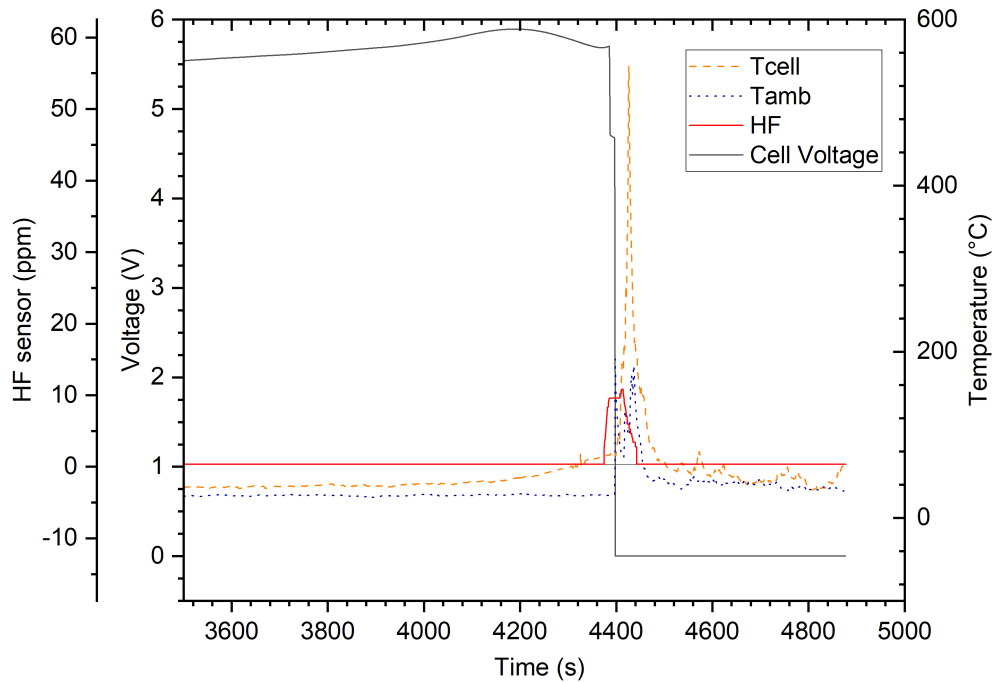
The results of overcharging experiment 1 were quite abrupt and due to the rapid flaming the gas emission sustained for a short time, the gas collection was thus inefficient. Hence it was decided to pierce the vent lightly beforehand, so the gas emissions could be smoother at the time of venting so that a detailed analysis of the emitted gases could be conducted. The pressure inside the cell was reduced due to the perforation and the venting started in a steady manner. In addition, the current supply was also interrupted this time when the cell started to visibly vent to check whether the fire could be avoided. The abuse test was started at 40 A and fixed at 50 A at an early stage. The voltage level was started at 3.7 V and peaks at 5.8 V and decays to 5.6 V before it drops due to cell failure.

Figure 23: Trace graphs of emissions during the experiment 2

(a) Trace of the overall parameters during the test

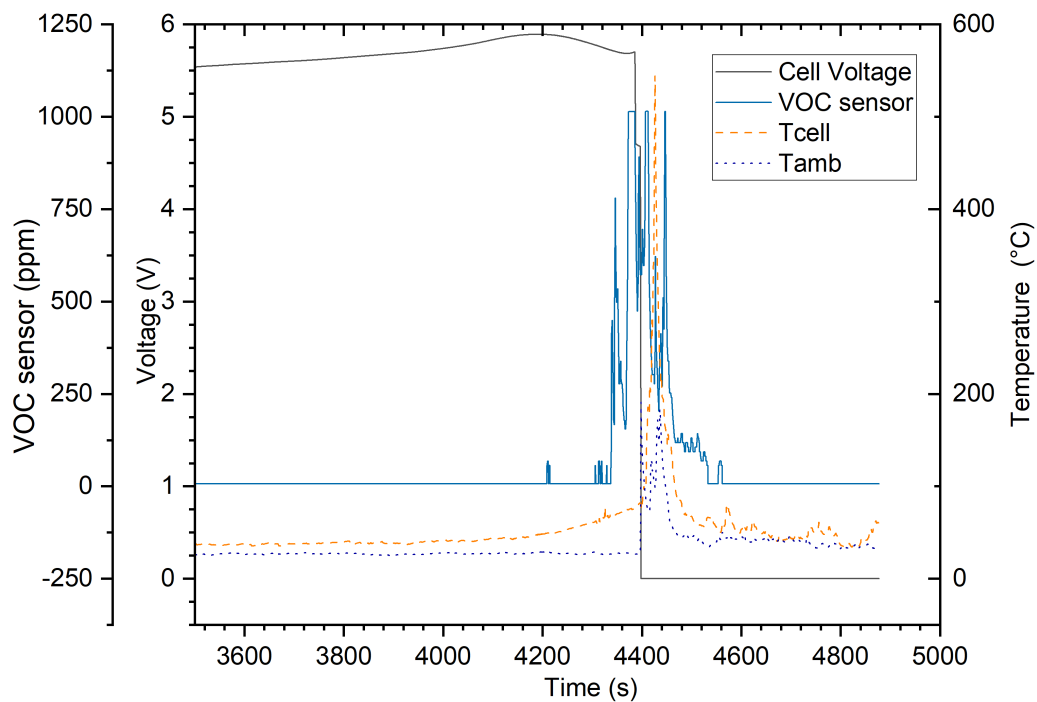


From figure 23a the voltage level and current levels are constant until venting. They drop quite simultaneously, however there is small difference in order of seconds. This voltage drop happened when the cell temperature was around 78°C. The CO sensor starts to receive signals quite early, before there is any relevant change in temperatures. At the time of flaming, the cell temperature reached around 544°C and the ambient temperature was measured at 191°C. The different gas events are discussed in the following.

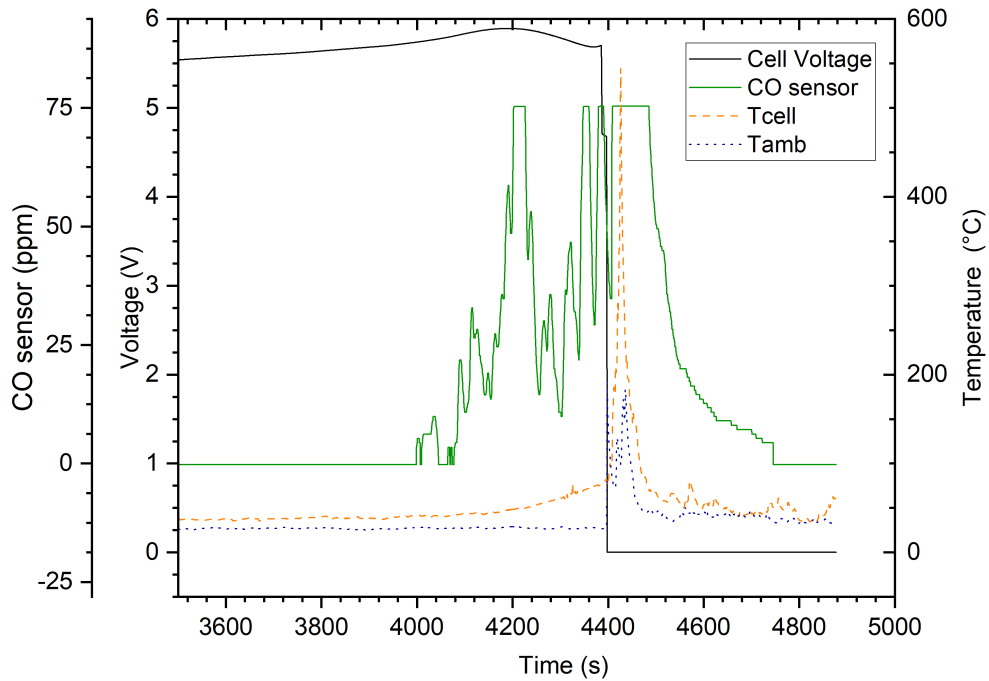


(b) Trace of hydrogen fluoride emission

The precedings of the emissions before failure can be seen in figures 23b and 23c. In fact the CO and VOC signals are seen quite early and onset is at around a cell temperature of 60°C. HF and methane emissions occur later. HF is reached around 11 ppm this time, whereas the volatile organic compound reading reaches the max reading limit of the signals which is over 1000 ppm.

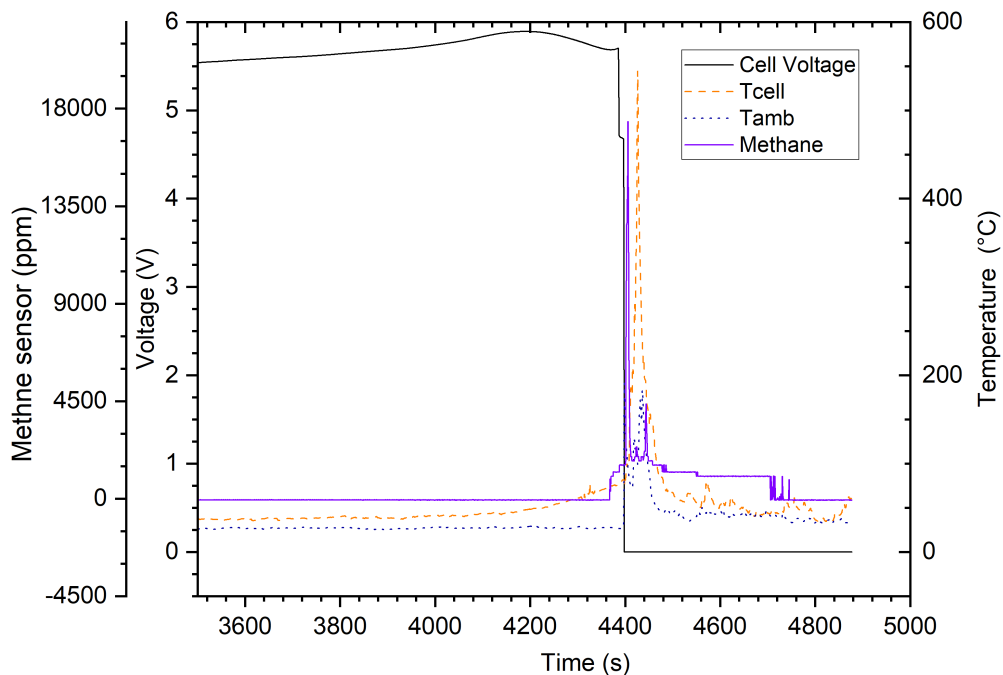


(c) Trace of Volatile Compounds emission



(d) Trace of Carbon monoxide emission

The onset signals for CO is very early during the increase of cell voltage, and the emissions started before the voltage breakdown started. As seen from figure 23d the CO emissions started when cell temperatures were normal around 20°C. So, CO is an early detection for this case. The CO emission starts about 6 minutes and peaks at 200 seconds before thermal runaway. However, the methane was detected after the voltage dropped to zero and was at 18000 ppm for a few seconds before it was consumed in the fire.



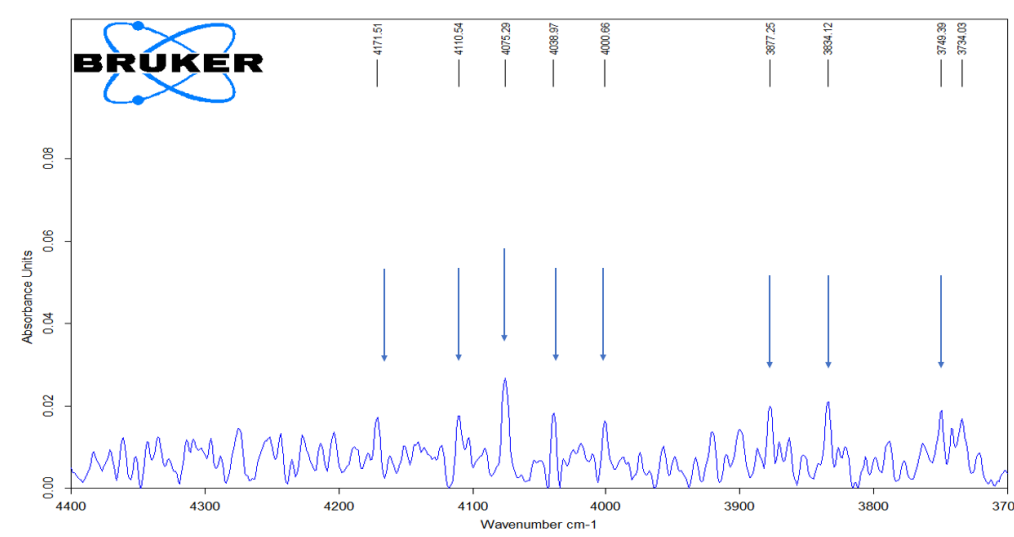
(e) Trace of methane emission

4.3.4 FTIR Spectrum analysis from experiment 2

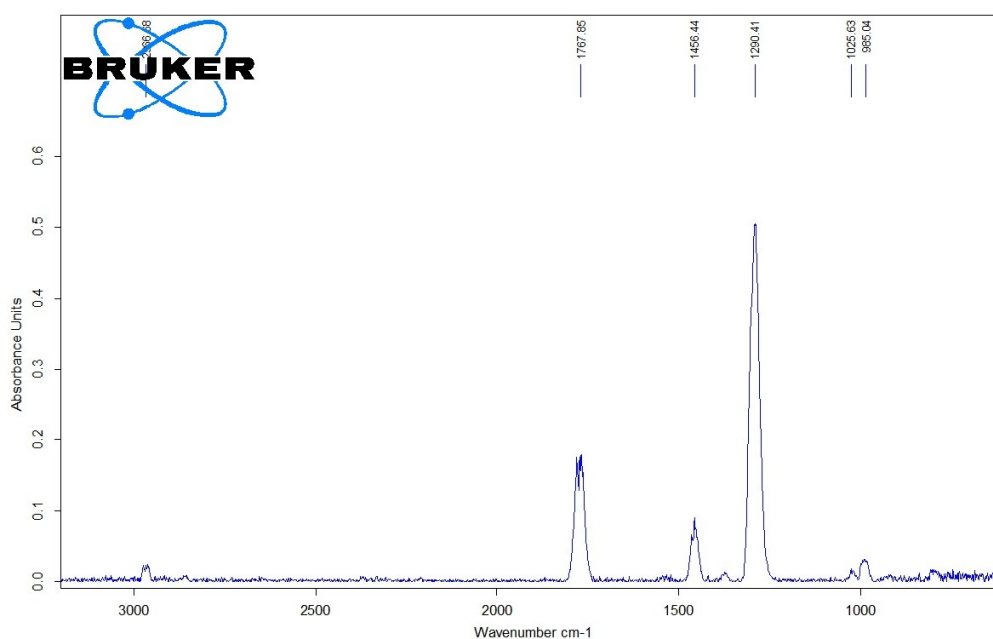
Figure 24a represents the FTIR spectrum from the vented gases particular to the hydrogen fluoride gas. The spectrum is weak but however the HF peaks are visible. The evenly spaced peaks between 3834 cm^{-1} and 4171 cm^{-1} in the figure correspond to the HF vibrational stretching and assignments are mentioned in table 7.

Figure 24: Gas emission FTIR spectrum from abuse test

(a) Hydrogen Fluoride gas emission spectrum at 4399 second

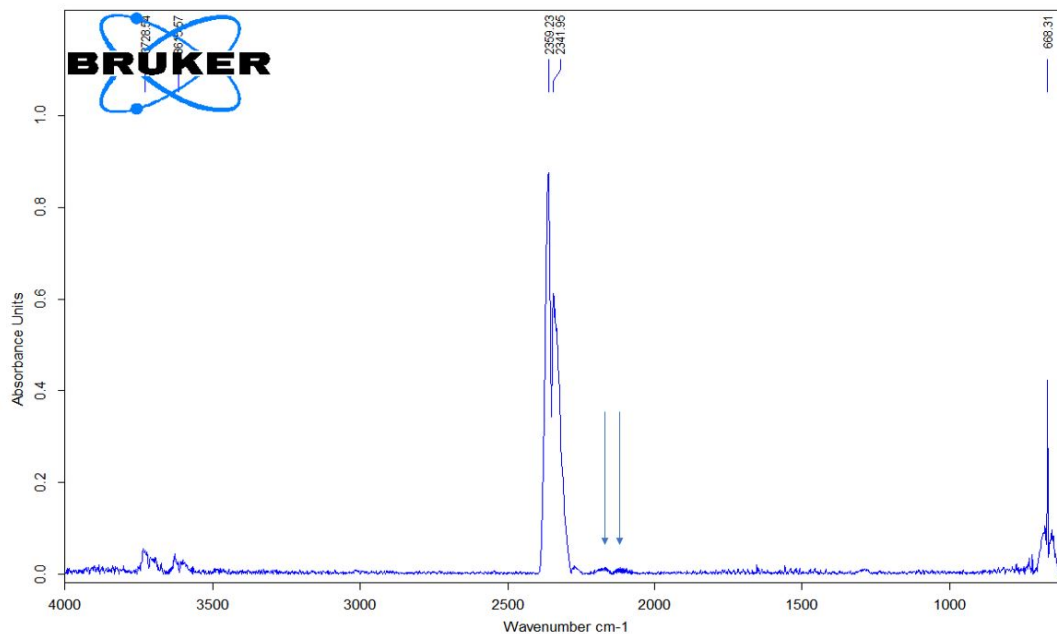


In figure 24b, very strong peaks are observed at 1290 cm^{-1} and 1767 cm^{-1} and with smaller peak at 1436 cm^{-1} . Hence all these peaks strongly prove the sole among DMC among organic solvents emissions during venting.

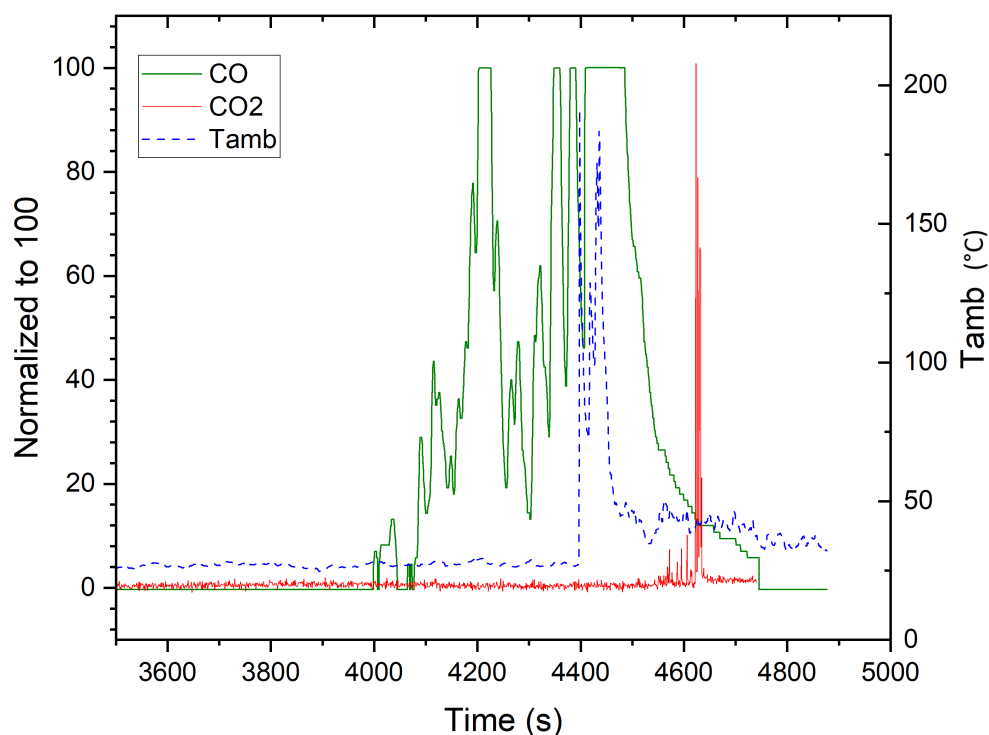


(b) Dimethyl carbonate gas emission spectrum at 4209 second

The very strong peaks at 2341 cm^{-1} and 2360 cm^{-1} are observed from the gas emission spectrum. These are the indicative peaks which precisely correlates to the wave-numbers of O-C-O stretching in table 7. The arrows represent the position of CO in 24c. CO_2 is also detected simultaneously to CO in the later stage, but with much lower signal which is observed in 24d.



(c) Carbon dioxide and carbon monoxide gas emission spectrum at 4111 second



(d) Normalized trace of carbon dioxide and carbon monoxide gases from FTIR at 2356 cm^{-1} and gas sensor respectively.

| Assignment | Wavenumber (cm ⁻¹) |
|---|--------------------------------|
| Vibration frequencies of DMC [32] | |
| CH ₃ -O stretching | 985 (+2) m |
| CH ₃ -O stretching | 992 m |
| O-C-O asymmetric stretching | 1290 vs (+3) |
| CH ₃ -O asymmetric deformation | 1453 vs |
| CH ₃ -O asymmetric deformation | 1463 vs |
| C=O stretching | 1767 (+1) |
| C=O stretching | 1780 (+1) |
| Vibration frequencies of HF [33] | |
| HF Stretching | 3656-4204 |
| Vibrational frequencies of CO₂ [34] | |
| O=C=O bending | 668 vs |
| O=C=O asymmetric stretching | 2341 vs |
| O=C=O asymmetric stretching | 2360 vs |
| O=C=O stretching + O=C=O bending | 3629 m |
| O=C=O symmetric and asymmetric stretching | 3727 m |
| Vibrational frequencies of CO [34] | |
| O≡C stretching | 2112 m |
| O≡C stretching | 2173 m |

Table 7: Assignments of spectrum bands from ATR spectrum of vented gas emissions from test cell 1 during abuse test

5 Conclusions

In this master thesis characterisation and abuse testing of high energy lithium-ion prismatic automotive battery cells was performed and reported. The electrical characterisation includes cycling the battery in potentiostatic and galvanostatic mode within prescribed voltage and current limits. The results from the cycling test showed that, out of 25 cycles the capacity of the battery fades or reduces minutely at the end of cycles. Another important observation is, the expansion of the cell case in central with respect to periphery region in the order hundreds of microns due to high current charging. The effect could be significant if considered on a battery system level where series of batteries are confined. Second, impedance spectroscopy was also carried to analyse the rise of any internal resistance. The measured internal resistance or impedance from the test cell was very low at the initial stage and remained low during cycling.

In addition, the physical characterisation of the interior cell materials is also performed. The cell and the components were weighed, once discharged and dismantled, the dimensions of both the electrodes and length of separators were measured and compared. From this type of characterisation, it was concluded that the area of the electrode plays a major role in capacity of the battery. But the test cell 1 and test cell 2 had similar areas whereas test cell 3 had lesser area. The increased capacity was supposed to be due to a different chemical composition or morphology of the electrode. Furthermore, with the assistance of differential scanning calorimetry equipment, thermal analysis was carried out on the extracted separator from all the test cells. The comparison with the commercial separators of single layer and multi layered type was brought forward. From the experimental results it was decided that most probably the separator material from the test cell was made from single layered porous polyethylene. Additionally, the X-ray diffraction method was used to investigate both the electrode materials. The results show that the major component of the anode material for all the test cells is graphite. The cathode material is composed of (NMC) which was also the expected outcome. The particular experiment setup was at its limit to distinguish more thorough and precise results. Hence in order to know the precise composition, more sophisticated experimental setup has to be used. The extracted electrolyte was examined with FTIR spectroscopy and it was deduced that the electrolyte contained DMC, EC and LiPF_6 . Deeper investigations are needed to know the presence of other chemical compounds.

Overcharge of test cell 1 was done to investigate whether the internal safety mechanism is able to prevent the failure and eventual thermal runaway. Two cells of the same type were overcharged beyond the limits. For the first cell the events were violent, with venting and fire occurring almost instantaneously which destroyed the cell completely. For the second cell, the vent was pierced beforehand and current supply was disconnected at the onset of visible venting. During this test, the cell caught fire after sometime although the current was disconnected. The emitted gases from the battery were sampled continuously and the chain of events was followed after venting. First, CO was detected. There was no fire at this stage. Then volatile organic compounds identified to be DMC via FTIR followed by HF and CH_4 were detected. Finally, a large fire appeared. The HF and CH_4 disappeared after fire but volatile organic compounds, CO and CO_2 could be detected for some time. Hence take away from this test is that CO could be used as an early warning for failure for this type of battery and for the scenario tested.

References

- [1] N. Nitta, F. Wu, J. T. Lee, and G. Yushin, “Li-ion battery materials: Present and future,” *Materials today*, vol. 18, no. 5, pp. 252–264, 2015.
- [2] Steven Loveday. “Tesla goes up in flames weeks after crash that didn’t involve fire.” (2022), [Online]. Available: <https://insideevs.com/news/591794/tesla-fire-wreckage-yard-three-weeks-after-crash/>. Retrieved June, 2022.
- [3] F. Larsson, P. Andersson, and B.-E. Mellander, “Lithium-ion battery aspects on fires in electrified vehicles on the basis of experimental abuse tests,” *Batteries*, vol. 2, no. 2, p. 9, 2016.
- [4] Green Car Congress. “Ratp withdraws 149 bolloré electric buses from service after two fires.” (2022), [Online]. Available: <https://www.greencarcongress.com/2022/04/20220430-ratp.html>. Retrieved May, 2022.
- [5] F. Larsson, J. Anderson, P. Andersson, and B.-E. Mellander, “Thermal modelling of cell-to-cell fire propagation and cascading thermal runaway failure effects for lithium-ion battery cells and modules using fire walls,” *Journal of the electrochemical society*, vol. 163, no. 14, A2854, 2016.
- [6] F. Larsson, P. Andersson, P. Blomqvist, and B.-E. Mellander, “Toxic fluoride gas emissions from lithium-ion battery fires,” *Scientific reports*, vol. 7, no. 1, pp. 1–13, 2017.
- [7] R. Schröder, M. Aydemir, and G. Seliger, “Comparatively assessing different shapes of lithium-ion battery cells,” *Procedia Manufacturing*, vol. 8, pp. 104–111, 2017.
- [8] One Charge. “Types of lithium batteries: Lithium cell format.” (2022), [Online]. Available: <https://www.onecharge.biz/lithium-cell-format/>. Retrieved May, 2021.
- [9] P. Svens, “Methods for testing and analyzing lithium-ion battery cells intended for heavy-duty hybrid electric vehicles,” Ph.D. dissertation, KTH Royal Institute of Technology, 2014.
- [10] J. B. Goodenough, “Evolution of strategies for modern rechargeable batteries,” *Accounts of chemical research*, vol. 46, no. 5, pp. 1053–1061, 2013.
- [11] B. Scrosati and J. Hassoun, “Lithium batteries: Current technologies and future trends,” *Functional Materials for Sustainable Energy Applications*, 573–600e, 2012.
- [12] D. Deng, “Li-ion batteries: Basics, progress, and challenges,” *Energy Science & Engineering*, vol. 3, no. 5, pp. 385–418, 2015.
- [13] I. Albinsson, *Dielectric and conductivity studies of polymer electrolytes*. Chalmers University of Technology, 1994.
- [14] E. Logan, E. M. Tonita, K. Gering, *et al.*, “A study of the physical properties of lithium-ion battery electrolytes containing esters,” *Journal of The Electrochemical Society*, vol. 165, no. 2, A21, 2018.
- [15] S. Bertilsson, F. Larsson, M. Furlani, I. Albinsson, and B.-E. Mellander, “Lithium-ion battery electrolyte emissions analyzed by coupled thermogravimetric/fourier-transform infrared spectroscopy,” *Journal of Power Sources*, vol. 365, pp. 446–455, 2017.
- [16] M. Tasumi, *Introduction to experimental infrared spectroscopy: Fundamentals and practical methods*. John Wiley & Sons, 2014.
- [17] C. P. Grey and D. S. Hall, “Prospects for lithium-ion batteries and beyond—a 2030 vision,” *Nature Communications*, vol. 11, no. 1, pp. 1–4, 2020.

- [18] J. R. Macdonald, "Impedance spectroscopy," *Annals of biomedical engineering*, vol. 20, no. 3, pp. 289–305, 1992.
- [19] H. Wondratschek, U. Müller, and U. internationale de cristallographie, *International tables for crystallography*. Wiley Online Library, 2004.
- [20] M. Razeghi, "Crystalline properties of solids," in *Fundamentals of Solid State Engineering*, Springer, 2019, pp. 51–84.
- [21] R. Sharma, D. Bisen, U. Shukla, and B. Sharma, "X-ray diffraction: A powerful method of characterizing nanomaterials," *Recent research in science and technology*, vol. 4, no. 8, 2012.
- [22] N. Pappas, "Calculating retained austenite in steel post magnetic processing using x-ray diffraction," 2006.
- [23] B. Fultz and J. M. Howe, *Transmission electron microscopy and diffractometry of materials*. Springer Science & Business Media, 2012.
- [24] A. Ali, Y. W. Chiang, and R. M. Santos, "X-ray diffraction techniques for mineral characterization: A review for engineers of the fundamentals, applications, and research directions," *Minerals*, vol. 12, no. 2, p. 205, 2022.
- [25] A. A. Bunaciu, E. G. UdriŞTioiu, and H. Y. Aboul-Enein, "X-ray diffraction: Instrumentation and applications," *Critical reviews in analytical chemistry*, vol. 45, no. 4, pp. 289–299, 2015.
- [26] P. Wang, Y. NuLi, J. Yang, and Y. Zheng, "Carbon-coated si-cu/graphite composite as anode material for lithium-ion batteries," *Int. J. Electrochem. Sci*, vol. 1, no. 3, pp. 122–129, 2006.
- [27] J. Y. Howe, C. J. Rawn, L. Jones, and H. Ow, "Improved crystallographic data for graphite," *Powder diffraction*, vol. 18, no. 2, pp. 150–154, 2003.
- [28] T. Pan, J. Alvarado, J. Zhu, *et al.*, "Structural degradation of layered cathode materials in lithium-ion batteries induced by ball milling," *Journal of The Electrochemical Society*, vol. 166, no. 10, A1964, 2019.
- [29] Q. Li, J. Chen, L. Fan, X. Kong, and Y. Lu, "Progress in electrolytes for rechargeable li-based batteries and beyond," *Green Energy & Environment*, vol. 1, no. 1, pp. 18–42, 2016.
- [30] J. Katon and M. Cohen, "The vibrational spectra and structure of dimethyl carbonate and its conformational behavior," *Canadian Journal of Chemistry*, vol. 53, no. 9, pp. 1378–1386, 1975.
- [31] B. Fortunato, P. Mirone, and G. Fini, "Infrared and raman spectra and vibrational assignment of ethylene carbonate," *Spectrochimica Acta Part A: Molecular Spectroscopy*, vol. 27, no. 9, pp. 1917–1927, 1971.
- [32] H. Bohets and B. J. van der Veken, "On the conformational behavior of dimethyl carbonate," *Physical Chemistry Chemical Physics*, vol. 1, no. 8, pp. 1817–1826, 1999.
- [33] P. Gerakines, W. Schutte, J. Greenberg, and E. F. van Dishoeck, "The infrared band strengths of h₂o, co and co₂ in laboratory simulations of astrophysical ice mixtures," *arXiv preprint astro-ph/9409076*, 1994.
- [34] G. Kuipers, D. Smith, and A. Nielsen, "Infrared spectrum of hydrogen fluoride," *The Journal of Chemical Physics*, vol. 25, no. 2, pp. 275–279, 1956.